Invited Paper

Multi-scale Modeling of Concrete Performance
Integrated Material and Structural Mechanics

Koichi Maekawa[1], Tetsuya Ishida[2] and Toshiharu Kishi[3]

Received 8 January 2003, revised 20 May 2003

Abstract

Multi-scale modeling of structural concrete performance is presented as a systematic knowledge base of coupled cementitious composites and structural mechanics. An integrated computational scheme is proposed for life-span simulation of reinforced concrete. Conservation of moisture, carbon dioxide, oxygen, chloride, calcium and momentum is solved with hydration, carbonation, corrosion, ion dissolution, damage evolution and their thermodynamic/mechanical equilibrium. The holistic system is verified by the reality.

1. Introduction

For sustainable development of gigantic urban universe where nature and people reside together, infrastructures are required to retain their performances over the long term. In order to construct durable and reliable social backbones, functionality, safety and their life shall be estimated on the basis of scientific and engineering knowledge. For present deteriorated infrastructures, a rational maintenance plan should be implemented in accordance with current situations. It is indispensable to grasp entire structural performances under predictable ambient and load conditions during the designated service life. The objective of this research is to develop multi-scale modeling of structural concrete performance and to realize a so-called lifespan simulator capable of predicting overall structural behaviors as well as constituent materials.

Figure 1 shows a schematic representation of the targeted multi-scale modeling of material science and structural mechanics. Macroscopic characters of concrete composites are rooted in micro-pore structures and thermodynamic states having much to do with durability. In turn, chemo-physical states of substances in nano~micro-pores are greatly associated with structural mechanics with damaging induced by loads and weather actions. For considering the practical use of knowledge, two sub-fields of structural mechanics and material science have been investigated with a couple of interacting engineering factors with a macroscopic feature of composites like uniaxial strength. Currently, much valuable knowledge is in our hands. In view of academia, the authors have recognized that it is natural to synthesize plenty of knowledge about concrete on a systematic platform like trees with leaves. The knowledge should not be mere archives or indexers, but quantitative estimation shall be drawn from it. Thus, overlaid multiple linkage is aimed on an info-technological basis.

For practice, multi-scale behavioral simulation of coupled constituent materials and structures is expected to serve engineers in charge of design, planning and policymaking. As a matter of fact, real maintenance issues require comprehension of materials, structures, construction and management. Thus, the computerized scheme based on holistic approach is sought by means of explicit mathematical formula originated from the past research.

This paper will propose one of the possible means to build up a systematic knowledge basis to amalgamate material and structural engineering. As a main discussion point is addressed to the system formation, some models of microphysical chemistry are forced to be somehow simplified. Doubtlessly, system competence significantly relies on its constituent elements. Thus, individual modeling shall be experimentally verified for continuous development as a quantitative knowledge for engineers.

2. Basic Computational Scheme

In principle, a distributed object-oriented scheme on open memory space is implemented as shown in **Fig. 2.** Chemo-physical and mechanical events in 3D extent are individually solved in a particular time step. The authors select the following kinematic chemo-physical and mechanical events (**Fig. 2**) with different geometrical scales of referential control volume (REV) where governing equations hold as,

(1) Cement heat hydration and thermal conduction (thermal conservation) – 10^{-6}~10^{-4} m scale

(2) Pore structure formation and moisture equilibrium/transport (water mass conservation) – 10^{-10}~10^{-6} m scale

(3) Free/bound chloride equilibrium and chloride ion transport (chloride ion conservation) – 10^{-8}~10^{-6} m scale

[1]Professor, University of Tokyo, Japan
E-mail: maekawa@concrete.t.u-tokyo.ac.jp
[2]Assistant Professor, University of Tokyo, Japan
[3]Associate Professor, University of Tokyo, Japan

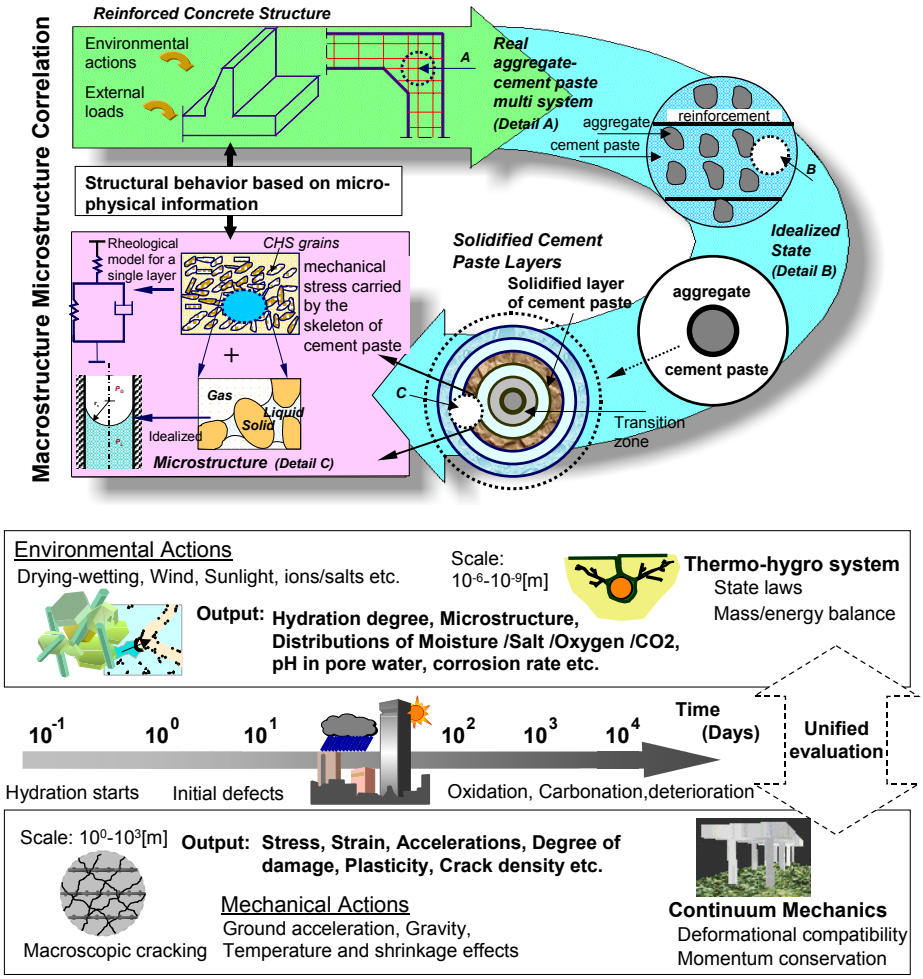

Fig. 1 Multi-scale scheme and lifespan simulation for materials and structures.

(4) Carbonation and dissolved carbon dioxide migration (CO_2/$Ca(OH)_2$ mass conservation) – 10^{-9}~10^{-6} m scale

(5) Corrosion of steel and dissolved oxygen transport (O_2/proton conservation) – 10^{-9}~10^{-6} m scale

(6) Calcium ion leaching from $Ca(OH)_2$ and transport (Ca^{++} ion + $Ca(OH)_2$ conservation) – 10^{-9}~10^{-6} m scale

(7) Chrome dissolution and migration (Cr ion mass conservation) – 10^{-9}~10^{-6} m scale

(8) Macro-damage evolution and momentum conservation (static/dynamic equilibrium) – 10^{-3}~10^{-0} m scale

Here, these events are not independent but mutually interlinked with each other. A complex figure of interaction is mathematically expressed in terms of state parameters commonly shared by each event. For example, Kelvin temperature and pore water pressure are seen in the modeling of cement hydration rate, moisture equilibrium, constitutive law of hardened cement paste, conductivity of carbon dioxide, bound and free chloride equilibrium, etc. In order to simultaneously solve these multi-scaled chemo-physical/mechanics, each event is sequentially processed with revising the state parameters commonly referred to and the computation is cycled till the whole conservation requirement is satisfied at each time step. Approximately 100 nonlinear governing equations to be simultaneously solved and their independent variables of the same numbers are summarized in the Appendix. In other words, concrete performance of micro and macro scales is characterized by these set of variables having multi-overlaid structures of cement composites. Individual chemo-physical events will be discussed subsequently.

Each sub-event is discretized in space by applying Galarkin's method of weighted residual function on finite element scheme. This three-dimensional multi-scale coupled system is built on the thermo-hydro physics coded by *DuCOM* for early aged concrete (Maekawa et al. 1999) and nonlinear mechanics FEM coded by *COM3* (Maekawa et al. 2003) for seismic performance assessment of reinforced concrete. The reason we select an object-oriented scheme is its stability of convergence and easy extensibility. In fact, soil foundation space, microorganism activity and electric potential field were easily overlaid on this system for further extension and are being investigated.

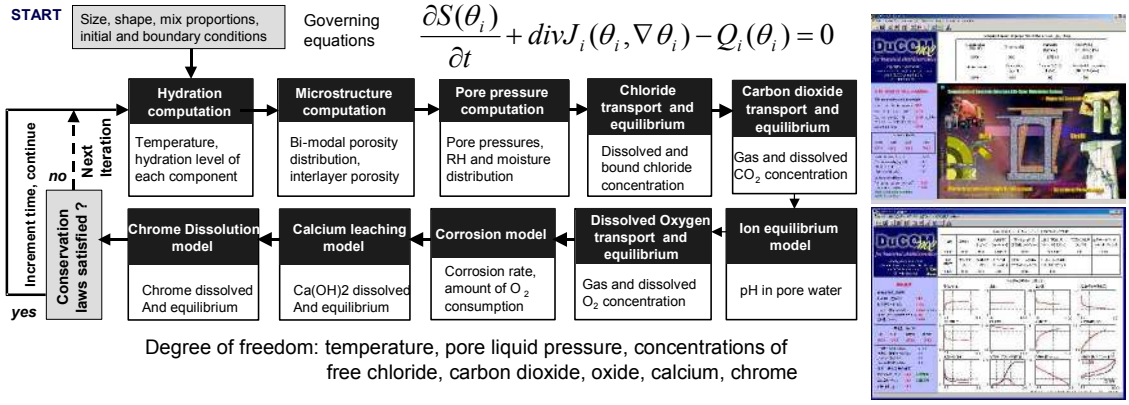

Fig. 2 (a) Sub-structure platform of ***Co***ncrete ***M***odel for ***Du***rability – DuCOM- (Maekawa et al. 1999, Ishida 1999).

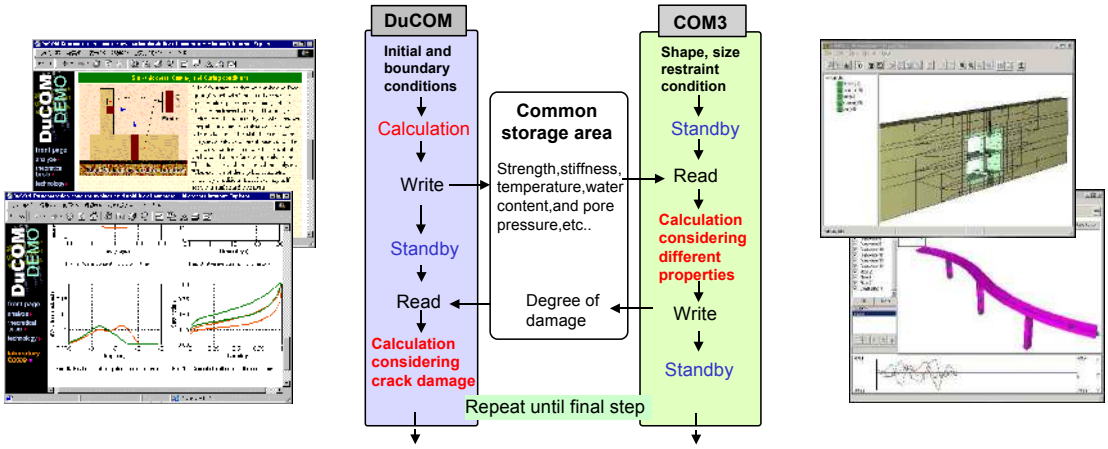

Fig. 2 (b) Integration of microphysics and macro-structural analysis (Maekawa et al. 1999, Ishida and Maekawa 2000, Maekawa et al. 2003).

3. Multi-Scale Modeling

3.1 Pore-Structure Model of Cement Paste – 10^{-10}~10^{-6} *m Scale* –

Computational modeling of varying micro-pore structures of hardening cement paste media is a central issue of multi-scale analysis. Moisture migration and durability related substances (in this study, calcium, chloride, dissolved CO_2 and O_2 are treated) and diffusion of gaseous phases are greatly governed by micro-pore structures. Without information of these mass transport and equilibrated thermo-dynamic states, we cannot predict hydration of cement, carbonation and corrosion of steel. Volumetric change caused by drying and stresses invoked are affected by the micro-pore moisture and the solidified skeleton mechanics of concrete. Here, the authors initiate multi-scale modeling with nm-μm scale hardening cement with CSH hydrates (Maekawa et al. 1999).

Suspended particles of cement are idealized spherical and representative unit cell consisting of a particle and water at the initial stage is defined as shown in **Fig. 3**. For simplicity, radius of individual cement particle is assumed constant equal to average representative. Cement hydration creates CSH grains inside and outside of the original spherical geometry. Inner product is thought to have no capillary distance between CSH grains. But, outside original sphere, gaps are formed in between CSH grains. In this study, this gap space surrounded by CSH grains is defined as capillary pores as shown in **Fig. 3**.

For statistically identifying micro-pores of nm~μm scales, the authors introduced the following hypothesis and computational assumption according to cement solid science earned in the past several decades.

(G1) The particle size and geometry of CSH grains are constant. (Volume to surface area ratio=19nm for OPC)

(G2) No capillary space is made inside the original sphere and porosity of outer product varies linearly (**Fig. 4**).

(G3) CSH grains contain interlayer pores and gel pores as shown in **Fig. 3**.

When we direct our attention to the inside of CSH grains, interlayer pores whose size is similar to that of a water molecule are identified. The authors further assume the following:

(I1) Total porosity of CSH grains is constant (0.28)

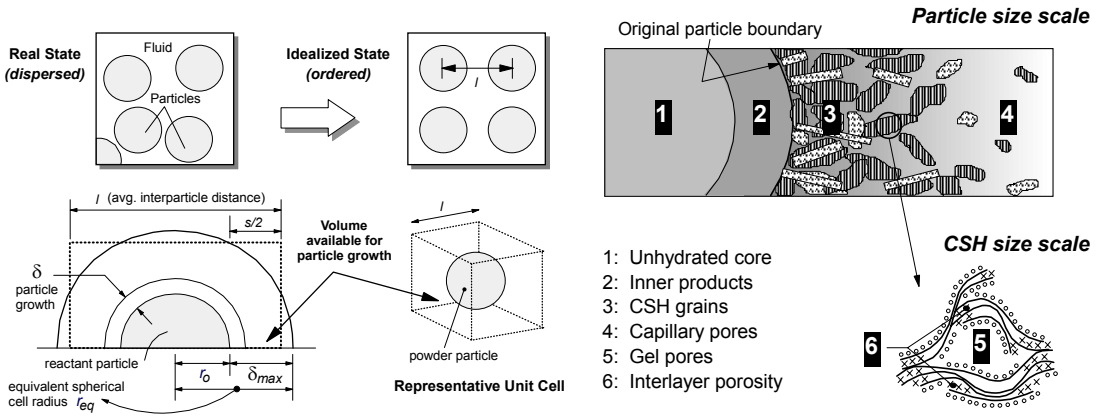

Fig. 3 Statistical modeling of micro-pore geometry and size for hardening cement paste.

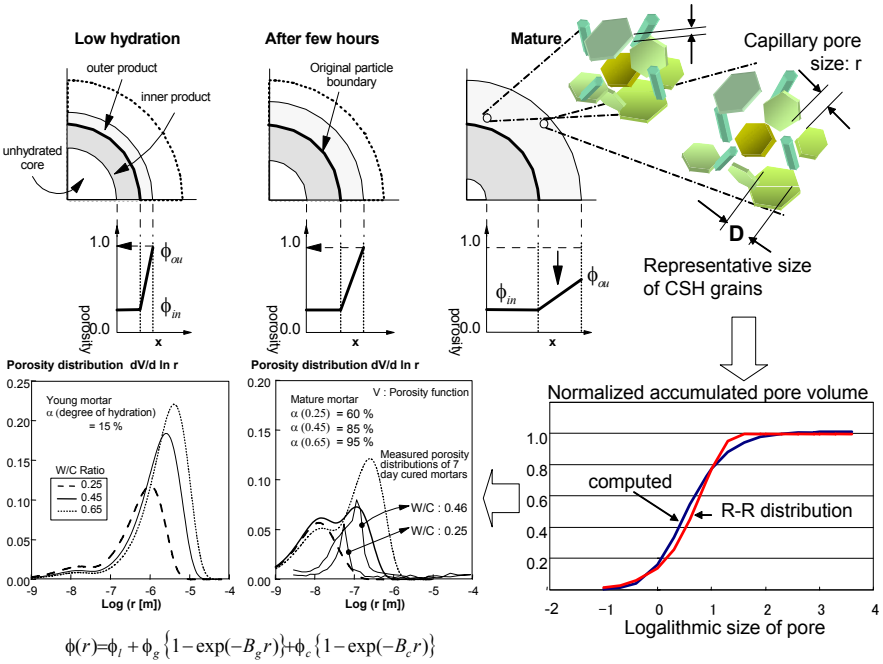

Fig. 4 Micro-pore development and statistical expression.

and the size of interlayer in CSH grains is assumed 2.8A.

(I2) The specific surface area of interlayer is 510m^2/g for OPC and that of gel pores is 40m^2/g as constant.

From hypothesis G1 and G2, the capillary pore size distribution can derive (**Fig. 4**). As capillary porosity at location '*x*' from the original boundary of the cement particle is proportional to the gap size '*r*' (capillary pore size) between CSH grains and assumed to linearly vary in space, we have,

$$\phi_c(x)=\frac{r}{D+r}=\left(\frac{x}{\delta_{\max}}\right)\phi_{ou} \tag{1}$$

where, D: size of CSH grains, δ_{max}: distance between the extreme radius of unit cell (REV) and the original boundary (**Fig. 3**), ϕ_{ou}: porosity at the extreme radius of the unit cell (**Fig. 3** and **Fig. 4**). Accumulated volume of capillary pores formed up to distance x is computed by integrating porosity with respect to location as,

$$Vx=\int_0^x \phi_c(x)4\pi(x+x_o)^2\,dx \tag{2}$$

Substitution of Eq. 1 into Eq. 2 yields,

$$Vx=A\left(\frac{1}{4}x^4+\frac{2}{3}x_o x^3+\frac{1}{2}x_o^2 x^2\right) \tag{3}$$

Since location x is nonlinearly related to the capillary pore size by Eq. (1), the accumulated volume of capillary pores can be implicitly obtained in terms of the pore size as shown in **Fig. 4** (in case of δ_{max}=1, x_o=1, ϕ_{ou} =1). Since the explicit expression of pore volume with respect to the pore size is convenient for computation, Raleigh-Ritz

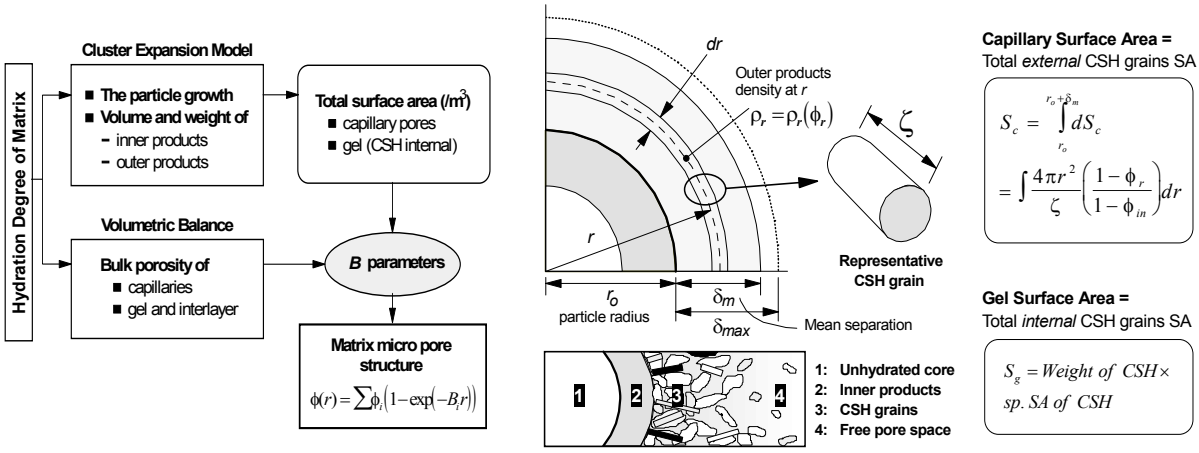

Fig. 5 Computation of varying surface area of hydrates and capillary pores.

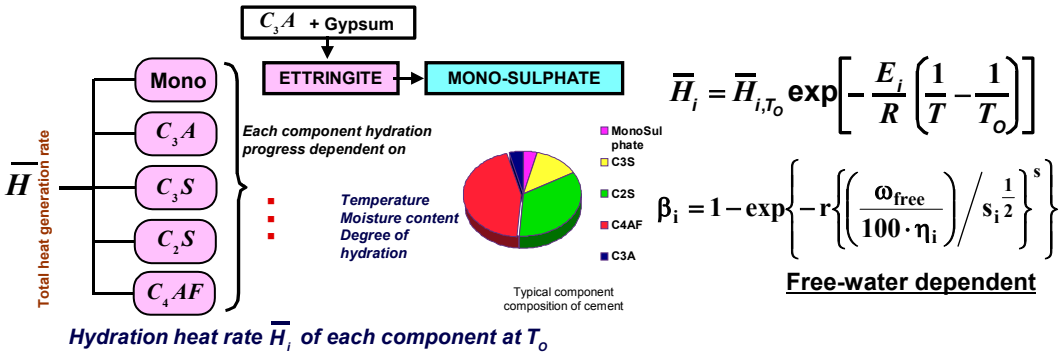

Fig. 6 Multi-mineral component model of cement hydration and heat generation.

(*R*-*R*) distribution function nearly equivalent to the statistical pore size distribution derived from Eq. 3 is accepted (**Fig. 4**) and the equivalent expression of entire micro-pore structures are proposed as,

$$\phi(r) = \phi_{lr} + \phi_{gl}\left(1-\exp\left(-B_{gl}r\right)\right) + \phi_{cp}\left(1-\exp\left(-B_{cp}r\right)\right) \qquad (4)$$

where, the same R-R distribution function is applied to the gel pores (the second term) and the size of interlayer pore (the first term) is assumed constant by hypothesis (I1). The porosity of each specific pore denoted by ϕ_{lr}, ϕ_{gl}, ϕ_{cp} in Eq. 4 is computed based upon the hypothesis stated above and the hydration degree. The sole parameter to specify the pore size distribution B can be uniquely decided by the surface area of each pore system. Provided that the micro-pore is of tubular geometry of random connection, the specific surface area denoted by S yields,

$$S = 2\phi\int r^{-1}dV = 2\phi\int_{r_{\min}}^{\infty} B\exp\left(-Br\right)d\ln r \qquad (5)$$

Thus, Raleigh-Ritz parameter B can be uniquely determined by S. As the specific surface area of gel is given by hypothesis (I2) as constant, B_{gl} is not variable during the hydration process but the porosity is solely increasing as hypothesis (G1) assumes. The surface area of capillary pores derives from hypothesis (G1) and (G2) by integrating the local surface area of capillary pores and mass equilibrium (**Fig. 5**). The surface area of capillary pores drastically varies in accordance with cement hydration and its mean size is decreasing. The detailed derivation of porosity and surface area of each pore system from hydration degree is presented in (Maekawa 1999) and the governing equations are summarized in Appendix.

The Multi-component cement hydration model by Kishi and Maekawa (1996, 1997) is used in this study. As cement consists of several minerals, the averaged activation energy is not constant in nature and the hydration pattern looks complex. In considering the engineering practice for different sorts of Portland cement and mixed cement with pozzolans, the authors computationally define referential hydration (heat) rate and activation energy of each mineral compound as shown in **Fig. 6**. Although each mineral activation is constant, apparently varying activation energy of cement, which is extracted from adiabatic temperature rise tests, can be simulated in terms of hydration degree. The effect of free water on hydration rate is modeled by hard shell concept of hydrated cluster. The detailed formulation is also lined up in Appendix.

3.2 Moisture Transport and Equilibrium – 10^{-10}~10^{-6} *m Scale* –

Moisture mass balance must be strictly solved in both vapor and condensed water. The conservation equation is expressed with capacity, conductivity and sink terms on the referential volume as shown in **Fig. 7** (Maekawa et al. 1999). Pore pressure of condensed water is selected as a chief variable so that both saturated and unsaturated states can be covered with perfect consistency. Another key issue here is that material characteristic parameters are variable with respect to micro-pore development.

Knudsen diffusion theory was applied for vapor transport and conductivity component is formulated based on vacant micro-pores where vapor can move as shown in **Fig. 7**. For liquid transport, random pore model described by percolation threshold was applied and its conductivity is computed based on the micro-pore distribution occupied by condensed water. Moisture transport in a porous body would be driven by temperature, pore pressure, and vapor pressure difference. In this study, total flux of moisture $\boldsymbol{J}$ is formulated as,

$$J = -\left(D_p \nabla P_l + D_T \nabla T\right) \tag{6}$$

where, D_p and D_T represent the macroscopic moisture conductivities with respect to pore pressure and temperature potential gradient, respectively. The conductivity D_p in Eq. 6 includes vapor diffusivity as well as liquid permeability, since vapor diffusivity and its gradient can be described together in the first term of the right hand side (**Fig. 7**). Under isothermal conditions (293[K]), vapor flux can be described as (Maekawa et al. 1999),

$$q_v = -\frac{\rho_v^{sat}\phi D_0}{\Omega}\int_{r_s}^{\infty}\frac{dV}{1+N_k}\nabla h \qquad N_k = \frac{l_m}{2\left(r-t_a\right)} \tag{7}$$

where, ρ_v^{sat}: vapor density under saturated condition [kg/m^3], ϕ: porosity, D_0: vapor diffusivity [m^2/s] in free atmosphere at 293 [K], Ω: parameter representing tortuosity of pore ($=(\pi/2)^2$), N_k: Knudsen number, V: pore volume [m^3], h: relative humidity, l_m: mean free path of a water molecule [m], and t_a: thickness of adsorbed layer [m]. In the model, factors reducing the apparent diffusivity of vapor are taken into account, such as complicated pore network, reduction of pore volume through which vapor movement can take place with increasing saturation and Knudsen diffusion.

When the vapor flux under various temperature conditions is solved, the gradient of relative humidity cannot be defined as its potential. In other words, relative humidity at different temperatures does not represent the driving force correctly, since the saturated vapor pressure depends on temperature, which leads to different relative humidity even though vapor density of the system is the same. Therefore, in order to generalize Eq. 7 for arbitrary temperature, the authors tailored the equation as (Ishida and Maekawa 2002),

$$q_v = -\frac{\phi D_0(T)}{\Omega}\int_{r_c}^{\infty}\frac{dV}{1+N_k}\nabla\rho_V = -D_v\nabla\rho_V$$
$$N_k = \frac{l_m}{2\left(r-t_a\right)} \tag{8}$$

The vapor flux described by Eq. 8 is driven by the gradient of absolute vapor density ρ_v of the system, instead of relative humidity. Here, absolute vapor density ρ_v corresponds to the product of relative humidity h and ρ_v^{sat} in Eq. 7. It has to be noted that vapor diffusivity has a strong dependence on temperature of the system. From a thermodynamic point of view, mass diffusivity under different temperature conditions can be derived by,

$$\frac{D_0(T_1)}{D_0(T_2)} = \left(\frac{T_1}{T_2}\right)^{3/2}\left(\frac{\Omega_{D,T2}}{\Omega_{D,T1}}\right) \tag{9}$$

where, $\Omega_{D,T1}$ and $\Omega_{D,T2}$ are collision integrals for mo-

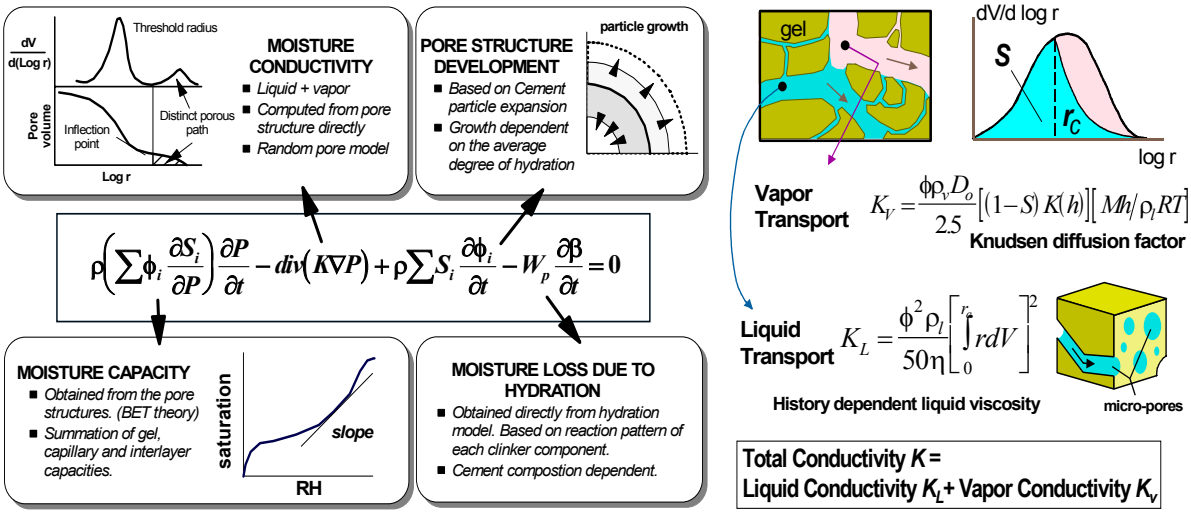

Fig. 7 Moisture conservation and transport based on statistical structural model of micro-pores.

lecular diffusion at temperature T_1 and T_2, respectively, which are functions of Boltzmann constant, temperature, and so on(Welty et al. 1969).

Next, the flux of liquid water q_l can be described as (Maekawa et al. 1999),

$$q_l = -\frac{\rho_l \phi^2}{50\eta}\left(\int_0^{r_c} r dV\right)^2 \nabla P_l = -K_l \nabla P_l \tag{10}$$

where, η is viscosity of fluid. It has been reported that the actual viscosity in the cementitious microstructure is far from the one of bulk water under ideal conditions. To account such a phenomenon, Chaube et al. proposed the following model based on the thermodynamics as (Maekawa et al. 1999),

$$\eta = \eta_i \exp\left(\frac{G_e}{RT}\right) \tag{11}$$

where, η_i: referential viscosity under ideal conditions and G_e: free energy of activation of flow in excess of that required for ideal flow conditions. Considering a pore-water and microstructure interaction, Gibbs free energy G_e has been formulated as a function of characteristics of pore structure and moisture history. In the proposed model, the different value of viscosity η_i is given according to temperature in a pore, whereas the authors use the same formulation to evaluate the Gibbs energy since the effect of temperature is implicitly considered by the original formula. Then, we have (Ishida and Maekawa 2002),

$$\begin{aligned} J &= -\left(D_p \nabla P_l + D_T \nabla T\right) \\ &= -\left\{ D_v \left(\frac{\partial \rho_v}{\partial P_l} \nabla P_l + \frac{\partial \rho_v}{\partial T} \nabla T \right) + K_l \nabla P_l + K_T \nabla T \right\} \\ &= -\left(D_v \frac{\partial \rho_v}{\partial P_l} + K_l \right) \nabla P_l - \left(D_v \frac{\partial \rho_v}{\partial T} + K_T \right) \nabla T \end{aligned} \tag{12}$$

In general, mass transport due to temperature gradient is known as the Soret effect or thermal diffusion that is represented by the last term of the right hand side, i.e., K_T·grad(T). However, contribution of thermal diffusion to the total flux has not been cleared in concrete engineering. Moreover, this phenomenon normally plays a minor role in diffusion compared with moisture transfer driven by pore pressure and vapor pressure gradient (Welty et al. 1969). Then, as the first approximation, the thermal diffusion is neglected in this study ($K_T \approx 0$).

The moisture capacity term enumerates moisture content with regard to the pore pressure. Quasi-thermo equilibrium is assumed at any time in nm~μm sized pores residing in REV. Vapor partial pressure can be obtained by equating Gibbs free energy of vapor to that of condensed water as,

$$P_l = \frac{\rho_l RT}{M_w} \ln \frac{p_{vap}}{p^*} \tag{13}$$

where, R: gas constant [J/mol.K], p^*: saturated vapor pressure [Pa], M_w: molecular mass of water [kg/mol] and ρ_l: density of liquid water [kg/m^3]. Under isothermal conditions, p_{vap}/p^* corresponds to relative humidity h inside pores.

By considering local thermodynamic and interface equilibrium, vapor and liquid interfaces would be formed in the pore structure due to pressure gradients caused by capillarity. When the interface is a part of an ideal spherical surface, the relation can be described by the Laplace equation as,

$$P_l = \frac{2\gamma}{r_s} \tag{14}$$

where, γ: surface tension of liquid water [N/m] and r_s: the radius of the pore in which the interface is created [m]. Based on the thermodynamic conditions represented by Eqs. 13 and 14, a certain group of pores whose radii is smaller than the specific radius r_s at which a liquid-vapor interface forms are completely filled with water, whereas larger pores remain empty or partially saturated.

If the porosity distribution of micro-pore structures is known, equations 13 and 14 allow us to obtain the amount of condensed water at a given relative humidity or absolute vapor pressure. By combining the above theory with the micro-pore structure distribution model, we evaluate the moisture profile under an isothermal condition (**Fig. 8**). In the model, adsorbed phases on the pore wall described by B.E.T. theory and trapped water due to inkbottle effect are taken into account as well as the condensed water (Maekawa et al. 1999, Ishida et al. 1998).

In Eq. 13, liquid density, surface tension, and saturated vapor pressure are temperature-dependent. For implicitly considering interdependency between temperature and moisture profile, liquid density and surface tension are given as nonlinear functions in terms of temperature based on measured values in experiments (Welty et al. 1969). With regard to the saturated vapor pressure varying with temperature inside pores, the authors apply the Clausius-Clapeyron equation as,

$$\frac{d \ln p}{dT} = \frac{\Delta H_{vap}}{RT^2} \tag{15}$$

where, ΔH_{vap} is the heat of vaporization [kJ/mol]. In this study, ΔH_{vap} is assumed to be constant (40.7 [kJ/mol]), since temperature variation is limited to the range from 273[K] to 373[K] in this study. By assuming the constant ΔH_{vap}, integral of Eq. 15 yields,

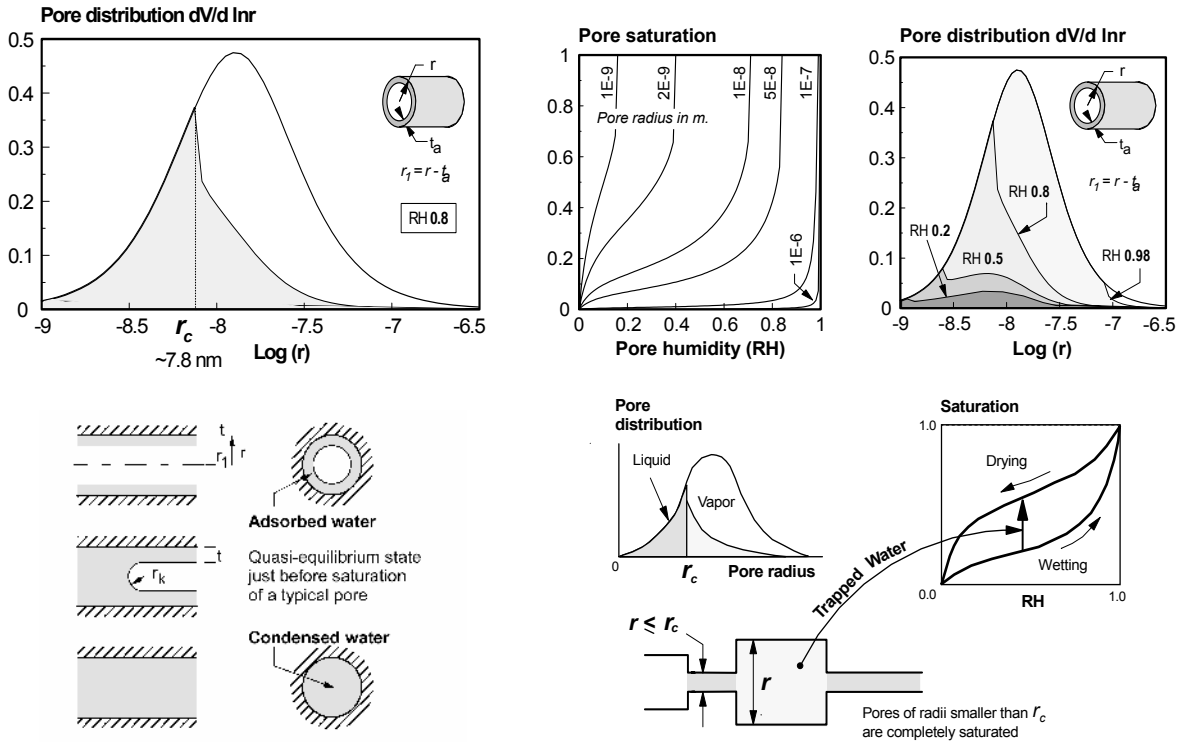

Fig. 8 Thermo-dynamic moisture equilibrium of condensed and adsorbed water in micro-gel and capillary pores.

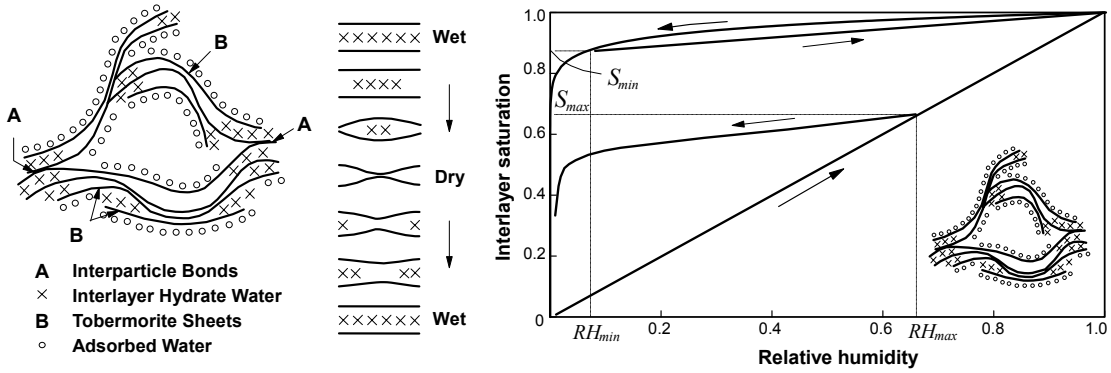

Fig. 9 Thermo-dynamic moisture equilibrium in micro-interlayer pores.

$$p_{vap} = p^* \exp\left(\frac{P_l M_w}{\rho_l RT}\right) = p_0 \exp\left\{-\left(\frac{\Delta H_{vap}}{R}\right)\left(\frac{1}{T}-\frac{1}{T_0}\right)\right\}\exp\left(\frac{P_l M_w}{\rho_l RT}\right) \quad (16)$$

where, p_0 and T_0 are the referential pressure and temperature, respectively.

From the above discussions, the relationship of pore pressure, saturated vapor pressure and absolute vapor pressure is specified. By combining the pore structure model with these formulations, moisture in terms of both vapor and liquid inside gel and capillary pores can be related to pore pressure.

Thermo-dynamics is hardly applied to behaviors of moisture inherent in interlayer pores with the angstrom scale but individual molecular dynamics is the matter. Here, empirically observed isotherm as shown in **Fig. 9** is used for evaluating total moisture capacity. Temperature is thought to be a key parameter especially for low water to cement ratio concrete having a great deal of interlayer pores. Currently, general modeling is under investigation.

3.3 Chloride Ion Transport and Equilibrium – 10^{-8}~10^{-6} *m Scale* –

Chloride transport in cementitious materials under usual conditions is an advective-diffusive phenomenon. In modeling, the advective transport due to bulk movement of pore solution phase is considered, as well as ionic diffusion due to concentration gradients. Mass balance for free (movable) chlorides can be expressed as (Ishida

1999a, Takeda and Ishida 2000) (**Fig. 10**),

$$\frac{\partial}{\partial t}(\phi S C_{cl}) + divJ_{Cl} - Q_{Cl} = 0,$$
$$J_{Cl} = -\frac{\phi S}{\Omega} D_{Cl} \nabla C_{Cl} + \phi S \boldsymbol{u} C_{Cl}, \quad (17)$$
$$\boldsymbol{u} = -\frac{K \nabla P}{\rho \phi S}$$

where, ϕ: porosity of the porous media, S: degree of saturation of the porous medium, C_{Cl}: concentration of ions in the pore solution phase [mol/l], J_{Cl}: flux vector of the ions [mol/m^2.s], $\boldsymbol{u}^T = [u_x\ u_y\ u_z]$ is the advective velocity of ions due to the bulk movement of pore solution phase [m/s], and Ω: tortuosity of pore-structures for a 3-D pore network which is uniformly and randomly connected. Tortuosity is a parameter that expresses a reduction factor in terms of chloride penetration rate due to complex micro-pore structure. In the current model, this parameter is determined by considering the geometric characteristics of pore structures based on experimental data for various water-to-cement ratios (Takeda and Ishida 2000, Takegami et al. 2002).

Material parameters shown in Eq. 17, such as porosity, saturation and advective velocity, are directly obtained based on the thermo-hydro physics. The advective velocity $\boldsymbol{u}$ is obtained from the pore pressure gradient ∇P and liquid water conductivity K which are calculated by moisture equilibrium and transport model, according to water content, micro pore structures, and moisture history. In the case of chloride ion transport in cementitious materials, S represents the degree of saturation in terms of free water only, as adsorbed and interlayer components of water are also present. It has to be noted here that the diffusion coefficient D_{Cl} in the pore solution may be a function of ion concentration, since ionic interaction effects will be significant in the fine microstructures at increased concentrations, thereby reducing the apparent diffusive movement driven by the ion concentration gradient (Gjørv and Sakai 1995).

This mechanism, however, is not clearly understood, so we neglect the dependence of ionic concentration on the diffusion process in the model. From several numerical sensitivity analyses, a constant value of 3.0×10^{-11} [m^2/s] is adopted for D_{Cl}. From the above discussions, the total diffusivity of concrete is described as the product of D_{Cl} and $\phi S/\Omega$, which depends on the achieved micro-structures (the initial mix and curing condition dependent variables) and moisture history.

As well-known, chlorides in cementitious materials have free and bound components. The bound components exist in the form of chloro-aluminates and adsorbed phases on the pore walls, making them unavailable for free transport. In this study, the relationship between free and bound components of chlorides is expressed by the equilibrium model proposed by Maruya et al. (1998), Takeda and Ishida (2000), and Takegami et al. (2002) as shown in **Fig. 10**. Here, the bound chlorides are classified into two phases: adsorbed and chemically combined components. Through these studies, it can be assumed that the amount of combined phases is approximately constant in terms of weight percent of hydrated gel products, whereas that of the adsorbed phase is strongly dependent on the constituent powder materials. For example, in the case of BFS, the amount of adsorbed phases becomes larger compared to the case of OPC, which leads to a higher binding capacity of BFS concrete and mortar. It means that the adsorbed component plays a major role in the chloride binding capacity of concrete.

By assuming local equilibrium conditions based on this relationship, the rate of binding or the change of free chloride to bound chloride per unit volume Q_{Cl} can be obtained. From the above discussions and formulations, the distribution of bounded and free chloride ions can be obtained without any empirical formula and/or intentional fittings, once mix proportions, powder materials, curing and environmental conditions are applied to the analytical system.

3.4 CO_2 Transport, Equilibrium and Carbonation – 10^{-9}~10^{-6} *m Scale* -

For simulating carbonation in concrete, equilibrium of gaseous and dissolved carbon dioxide, their transport, ionic equilibriums and carbonation reaction process are formulated on the basis of thermodynamics and chemical equilibrium theory by Ishida and Maekawa (2001). Mass balance condition for dissolved and gaseous carbon dioxide in porous medium can be expressed as,

$$\frac{\partial}{\partial t}\{\phi[(1-S)\cdot\rho_{gCO_2} + S\cdot\rho_{dCO_2}]\} + divJ_{CO_2} - Q_{CO_2} = 0 \quad (18)$$

where, ρ_{gCO2}: density of CO_2 gas [kg/m^3], ρ_{dCO2}: density of dissolved CO_2 in pore water [kg/m^3], J_{CO2}: total flux of dissolved and gaseous CO_2 [kg/m^2.s]. The local equilib-

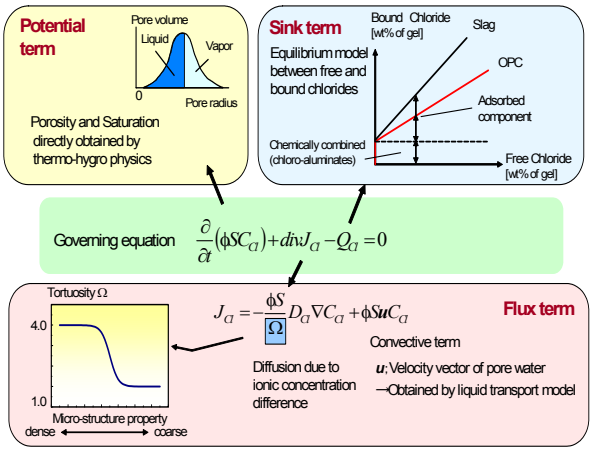

Fig. 10 Governing equation and constitutive models for chloride ion.

rium of gaseous and dissolved carbon dioxide is represented by Henry's law, which states the relation of gas solubility in pore water and the partial gas pressure. CO_2 transport is considered in both phases of dissolved and gaseous carbon dioxide. By considering the effect of Knudsen diffusion, tortuosity and connectivity of pores on the diffusivity, Fick's first law of diffusion yields the flux of CO_2 as,

$$J_{CO_2} = -\left(D_{dCO_2}\nabla\rho_{dCO_2} + D_{gCO_2}\nabla\rho_{gCO_2}\right),$$
$$D_{dCO_2} = \frac{\phi D_0^d}{\Omega}\int_0^{r_c} dV \quad D_{gCO_2} = \frac{\phi\cdot D_0^g}{\Omega}\int_{r_c}^{\infty}\frac{dV}{1+N_k} \tag{19}$$

where, D_{gCO2}: diffusion coefficient of gaseous CO_2 in porous medium[m^2/s], D_{dCO2}: diffusion coefficient of dissolved CO_2 in porous medium[m^2/s], D_0^g: diffusivity of CO_2 gas in a free atmosphere[m^2/s], D_0^d: diffusivity of dissolved CO_2 in pore water [m^2/s], V: pore volume, r_c: pore radius in which the equilibrated interface of liquid and vapor is created, N_k: Knudsen number, which is the ratio of the mean free path length of a molecule of CO_2 gas to the pore diameter. Knudsen effect on the gaseous CO_2 transport is not negligible in low RH condition, since the porous medium for gas transport becomes finer as relative humidity decreases. As shown in Eq. 19, the diffusion coefficient D_{dCO2} is obtained by integrating the diffusivity of saturated pores over the entire porosity distribution, whereas D_{gCO2} is obtained by summing up the diffusivity of gaseous CO_2 through unsaturated pores. Substitution of porosity saturation S for the integrals in the above equation in order to generalize the expression for an arbitrary moisture history gives,

$$D_{dCO_2} = \frac{\phi S^n}{\Omega}D_0^d,\ D_{gCO_2} = \frac{\phi\cdot D_0^g}{\Omega}\frac{(1-S)^n}{1+l_m/2(r_m-t_m)} \tag{20}$$

where, n is a parameter representing the connectivity of the pore structure, and might vary with the geometrical characteristics of the pores (Ishida and Maekawa 2001). In the model, through sensitivity analysis, n is tentatively assumed to be 4.0, which is the most appropriate value for expressing the reduction of CO_2 diffusivity with the decrease of relative humidity (**Fig. 11(a)**). In Eq. 19, the integral of the Knudsen number is simplified so that it can be easily put into practical computational use; r_m is the average radius of unsaturated pores, and t_m is the thickness of adsorbed water layer in the pore whose radius is r_m.

Q_{CO2} in Eq. 18 and Eq. 21 is a sink term that represents the rate of CO_2 consumption due to carbonation [kg/m^3.s]. The rate of CO_2 consumption can be expressed by the following differential equation, assuming that reaction is of the first order with respect to Ca^{2+} and CO_3^{2-} concentrations as,

$$Ca^{2+} + CO_3^{2-} \rightarrow CaCO_3,$$
$$Q_{CO_2} = \frac{\partial\left(C_{CaCO_3}\right)}{\partial t} = k[Ca^{2+}][CO_3^{2-}] \tag{21}$$

$$H_2O \leftrightarrow H^+ + OH^-$$
$$H_2CO_3 \leftrightarrow H^+ + HCO_3^- \leftrightarrow 2H^+ + CO_3^{2-}$$
$$Ca(OH)_2 \leftrightarrow Ca^{2+} + 2OH^-$$
$$CaCO_3 \leftrightarrow Ca^{2+} + CO_3^{2-} \tag{22}$$

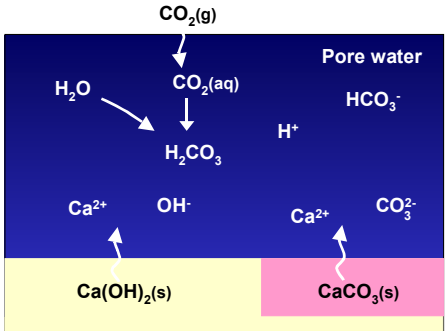

Fig. 11(b) Ion equilibrium in pore water.

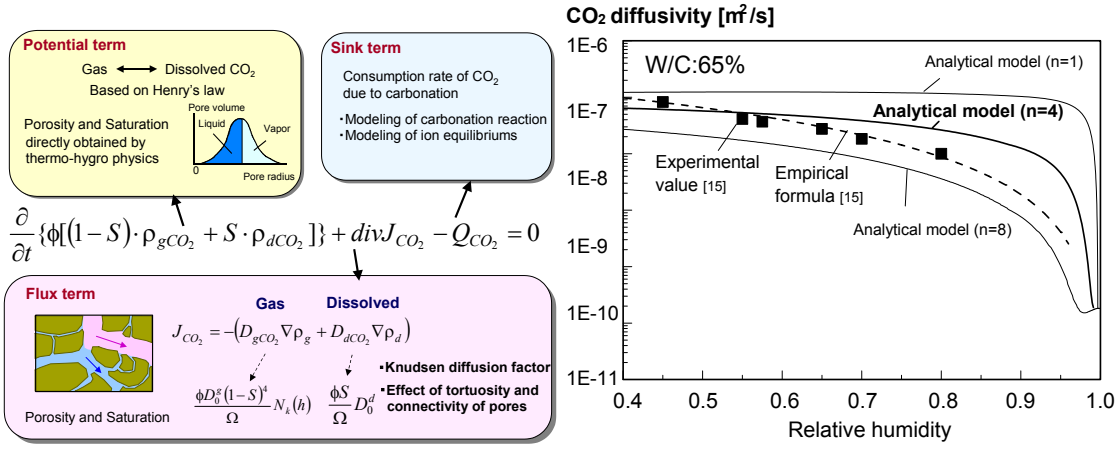

Fig. 11(a) Relationship between CO_2 diffusivity and relative humidity.

where, C_{CaCO3}: concentration of calcium carbonate, k is a reaction rate coefficient. In this paper, a unique coefficient is applied (k=2.08 [l/mol.sec]), although the reaction rate coefficient involves temperature dependency.

In order to calculate the rate of reaction with Eq. 21, it is necessary to obtain the concentration of calcium ion and carbonic acid in the pore water at an arbitrary stage. In this study, we consider the ion equilibriums; dissociation of water and carbonic acid, and dissolution and dissociation of calcium hydroxide and calcium carbonate as above. Here, the presence of chlorides is not considered, although chloride ions are likely to affect the above equilibrium conditions. The formulation including chlorides remains a subject for future study.

As shown in Eq. 22, carbonation is an acid-base reaction, in which cations and anions act as a Brönsted acid and base, respectively. Furthermore, the solubility of precipitations is dependent on the pH of the pore solutions. Therefore, for calculating the ionic concentration in the pore solutions, the authors formulated an equation with respect to protons [H^+], according to the basic principles on ion equilibrium; laws of mass action, mass conservation, and proton balance in the system (Freiser and Fernando 1963, Ishida and Maekawa 2001). In use of the equation, the concentration of protons in pore solutions can be calculated at an arbitrary stage, once the concentration of calcium hydroxide and that of carbonic acid before dissociation are given.

It has been reported that micro-pore structure is changed due to carbonation. In this paper, the authors use the empirical formula proposed by Saeki et al. (1991) as,

$$\begin{aligned} \phi' &= \phi\left(R_{Ca(OH)_2}\right) \quad \left(0.6 < R_{Ca(OH)_2} < 1.0\right) \\ \phi' &= 0.5 \cdot \phi \qquad \left(R_{Ca(OH)_2} \le 0.6\right) \end{aligned} \tag{23}$$

where, ϕ': porosity after carbonation, $R_{Ca(OH)2}$: the ratio of the amount of consumed $Ca(OH)_2$ for the total amount of $Ca(OH)_2$.

3.5 Oxygen Transport and Micro-cell Based Corrosion Model – 10^{-9}~10^{-6} *m Scale* -

In this section, a general scheme of a micro-cell corrosion model is introduced based on thermodynamic electro-chemistry (Ishida 1999a). Corrosion is assumed to occur uniformly over the surface areas of reinforcing bars in a referential finite volume, whereas formation of pits due to localized attack of chlorides and corrosion with macro cell remains for future study. **Fig. 12(b)** shows the flow of the corrosion computation. When we consider the micro-cell based corrosion, it can be assumed that the anode area is equal to that of the cathode and they are not separated from each other. Then, electrical conductivity of concrete, which governs the macroscopic transfer of ions in pore water, is not explicitly treated.

First of all, electric potential of corrosion cell is obtained from the ambient temperature, pH in pore solution and partial pressure of oxide, which are calculated by other subroutine in the system. The potential of half-cell can be expressed with the Nernst equation as (West 1986),

$$\begin{aligned} &\mathrm{Fe(s)} \rightarrow \mathrm{Fe^{2+}(aq)} + e\mathrm{(Pt)} \\ &E_{Fe} = E^{\Theta}_{Fe} + \left(RT/z_{Fe}F\right)\ln h_{Fe^{2+}} \\ &\mathrm{O_2(g)} + 2\mathrm{H_2O(l)} + 4e\mathrm{(Pt)} = 4\mathrm{OH^-(aq)} \\ &E_{O_2} = E^{\Theta}_{O_2} + \left(RT/z_{O_2}F\right)\ln\left(P_{O_2}/P^{\Theta}\right) \\ &\qquad - 0.06\,pH \end{aligned} \tag{24}$$

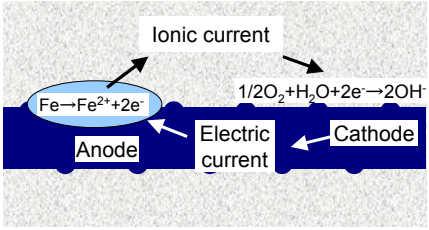

Fig. 12(a) Modeling of steel corrosion.

where, E_{Fe}: standard cell potential of Fe, anode (V, SHE), E_{O2}: standard cell potential of O_2, cathode (V, SHE), E^{Θ}_{Fe}: standard cell potential of Fe at 25ºC (=-0.44V,SHE), E^{Θ}_{O2}: standard cell potential of O_2 at 25ºC (=0.40V,SHE), z_{Fe}: the number of charge of Fe ions (=2), z_{O2}: the number of charge of O_2 (=2), P^{Θ}: atmospheric pressure. By assuming an ideal condition, we neglect the solution of other ions in pore water on the half-cell potentials. Further study is intended in the multi-scale scheme.

Next, based on thermo-dynamic conditions, the state of passive layers is evaluated by the Pourbaix diagram, where steel corrodes, areas where protective oxides from, and an area of immunity to corrosion depending on pH and the potential of the steel. From the electric potential and the formation of passive layers, electric current that involves chemical reaction can be calculated so that conservation law of electric charge should be satisfied in a local area (**Fig. 13(a)**). The relationship of electric current and voltage for the anode and cathode can be expressed by the following Nernst equation as,

$$\begin{aligned} &\eta^a = \left(2.303RT/0.5 \cdot z_{Fe}F\right)\log\left(i_a/i_0\right), \ \eta^c \\ &= -\left(2.303RT/0.5 \cdot z_{O_2}F\right)\log\left(i_c/i_0\right) \end{aligned} \tag{25}$$

where, η^a: overvoltage at anode [V], η^c: overvoltage at cathode [V], F: Faraday's constant, i_a: electric current density at anode [A/m^2], i_c: electric current density at cathode [A/m^2]. Corrosion current I_{corr} can be obtained as the point of intersection of two lines.

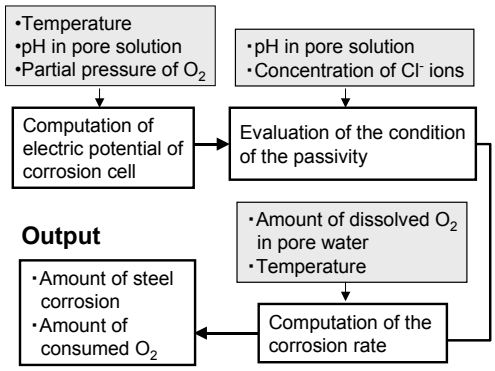

Fig. 12(b) Overall scheme of corrosion computation.

The existence of a passive layer reduces the corrosion progress. In this model, this phenomenon is described by changing the Tafel gradient (**Fig. 13(b)**). When chlorides exist in the system, the passive region hitherto occupied by Fe_3O_4 will disappear. In addition, the protective region of Fe_2O_3 will be divided into two regions, the lower of which corresponds to truly passive behavior and the upper to an unstable situation in which localized breakdown to pitting attack becomes possible (West 1986). Although the chloride induced corrosion may involve such a localized attack, an average treatment was introduced in this work, as shown in **Fig. 13(b)**. It has been reported from past researches that, as chlorides increase around reinforcing bars, current density of corrosion becomes larger due to the breakdown of passive films (Broomfield 1997). In this research, we assume that the anodic Tafel gradient would become smaller with higher concentration of chlorides. It has been also reported by Broomfield (1997) that there is a chloride threshold for starting corrosion. When the chloride concentration exceeds a concentration of 0.2% total chloride by weight of cement, corrosion is observed. In this research, the chloride threshold is specified in terms of the amount of free chloride existing in the pore water, and a value of 0.04 [wt% of cement] was given. This threshold value of free chloride was obtained from the chloride equilibrium model in **Fig. 10** by giving a typical concrete mix proportion with ordinary portland cement used. It is expected that when a lot of chlorides already exist, the rate of corrosion does not increase any more even though new chlorides migrate from the environment. In the model, when the concentration of free chlorides exceeds 0.4 [wt% of cement], the rate of corrosion is assumed to be equivalent to the corrosion rate of the steel without passive films.

When the amount of oxygen supplied to the reaction is not enough, corrosion rate would be controlled by diffusion process of oxygen (**Fig. 13(c)**). By coupling with an oxygen transport model, this phenomenon can be logically simulated. Current density i_{corr}, which is obtained as the intersection of anodic and cathodic polarization curve, corresponds to the corrosion under sufficient availability of oxygen (**Fig. 13(a)**). When oxygen supply shortens, the rate of corrosion will be limited by the slow diffusion of oxygen. A limited value of current density i_L can be expressed as,

$$i_L / z_{\mathrm{Fe}} F = \mathrm{O}_2^{\mathrm{sup}} \tag{26}$$

where, O_2^{sup}[mol/m^2.s] is the amount of oxygen supplied to the surface of metal, which is obtained by the equilibrium and transport model for oxygen discussed below. In this research, the rate of corrosion under diffusion control of oxygen i_{corr}[A/m^2] is assumed to be as (**Fig. 13(c)**),

$$i_{corr} = i_L \tag{27}$$

The potential difference between the anode and cathode corresponds to the concentration polarization.

Fig. 14 summarizes the formulation of the key governing equation, which is almost the same as that of carbon dioxide (Ishida and Maekawa 2001, Maekawa and Ishida 2002). Finally, using the Faraday's law, electric current of corrosion is converted to the rate of steel corrosion. These models derive from thermodynamic electrochemistry. Further development and improvement

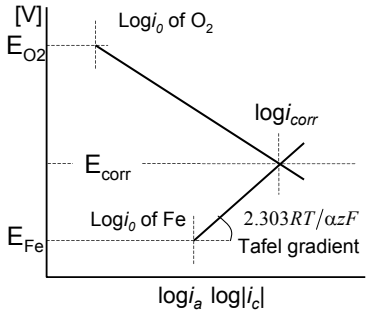

Fig. 13(a) Relationship of electric current and voltage for anode and cathode

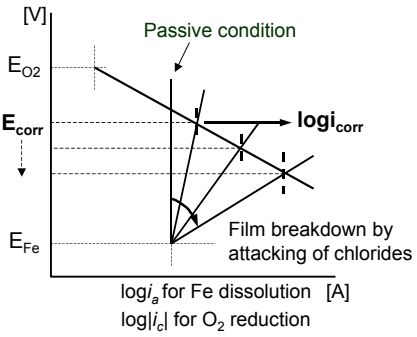

Fig. 13(b) Rate of corrosion accelerated by chloride migration

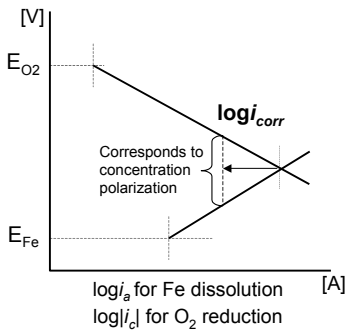

Fig. 13(c) Rate of corrosion under O_2 diffusion control

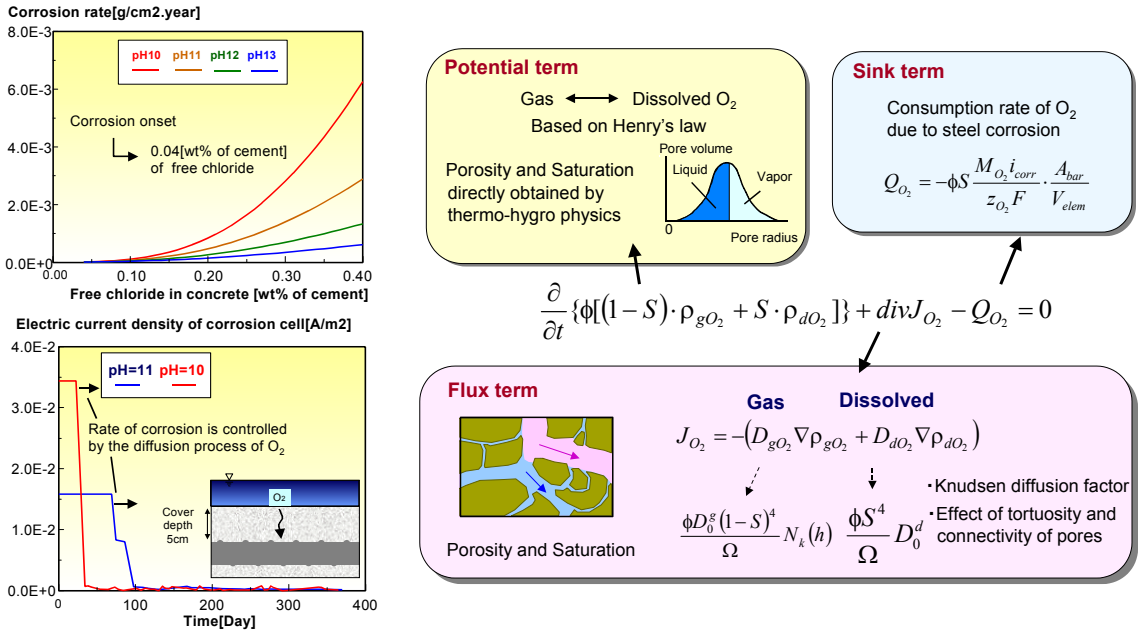

Fig. 14 Oxygen diffusion model linked with micro-corrosion of steel.

are still needed thorough various verification of corrosion phenomena in real concrete structures.

3.6 Calcium Ion Transport and Leaching – 10^{-9}~10^{-6} *m Scale* -

Calcium is one of the main chemicals and in pore solution, Ca^{2+} is equilibrated with $Ca(OH)_2$ solids and other ionic substances as stated in Eq. 22 and the Appendix in detail. Calcium leaching may change pore structures due to lost $Ca(OH)_2$ and long-term performance of cementitious solids would be influenced especially when exposed to pure water. Similar to chloride conservation in Eq. 22, we have,

$$\frac{\partial}{\partial t}\left(\phi S C_{ca}\right) + divJ_{ca} - Q_{ca} = 0,$$
$$J_{ca} = -\frac{\phi S}{\Omega} D_{ca} \nabla C_{ca} + \phi S \boldsymbol{u} C_{ca}, \quad \boldsymbol{u} = -\frac{K \nabla P}{\rho \phi S} \tag{28}$$

where, C_{ca}: calcium ion concentration, D_{ca}: diffusivity of Ca ion, Q_{ca}: dissolution rate. The saturated calcium ion concentration can be computed by Eq. 22 and solution product constant in Appendix with pH value. Then, Q_{ca} is given as the rate of dissolved ion concentration. In considering much smaller solubility, calcium dissolution from CSH hydrates is not considered in this study. In the same manner, chrome dissolution can be incorporated in the multi-scale platform, too.

3.7 Mechanics of Young Concrete before Cracking – 10^{-6} ~10^{-2} *m Scale* -

Degree of hydration and moisture in micro-pores greatly influences the solid mechanics of cementitious composites. Constitutive modeling has been proposed with respect to stresses/strains and the micro-pore related solid properties of young concrete composites have been considered in terms of varying elasticity and creep coefficients under specified ambient conditions. This macroscopic expression of micro-pore development makes practical application possible and has brought great advantage in the past.

Herein, a high level engineering judgment is required on such as ambient related parameters and 3D shape of structural geometry, since the local moisture conditions and micro-pore development are not explicitly known in computation. On this issue, the multi-scale scheme can explicitly deal with the full coupling of thermo-dynamic equilibrium of moisture and constitutive modeling of solid with micro-pores. The authors present a trial modeling of cement concrete composites whose micro/meso level solid mechanics is coupled with the nano/micro pore structures and thermo-dynamics of microclimate (Ishida et al. 1999b, Mabrouk et al. 1998 and 2000).

As the volume of cement paste matrix is highly associated with moisture migration unlike aggregates, volumetric interaction of aggregate elastic particles and paste matrix is one of key issues when we construct overall space-averaged constitutive modeling of concrete composite. On the other hand, shear deformational mechanics is thought greatly governed by matrix with less contribution of suspended aggregates. Then, the authors firstly apply mode separation similar to elasto-plastic and fracturing model of concrete (Maekawa et al. 2003) and secondly, we compose them into unified constitutive modeling for structural analysis.

3.7.1 Particle dispersion and solidification

Aggregate particles can be modeled as a suspended elastic body by surrounding cement paste as shown in **Fig. 15**. Local stresses developing in both aggregates and cement paste are non-uniform. Here, let us define the referential volume (REV) whose scale is 1-5cm including several gravels and lots of sands. The volumetric virtual work principle yields equilibrium of stress components and compatibility of strain fields on this REV as,

$$\begin{aligned} \bar{\sigma}_o &= \rho_{ag}\bar{\sigma}_{ag} + \rho_{cp}\bar{\sigma}_{cp} \\ \bar{\varepsilon}_o &= \rho_{ag}\bar{\varepsilon}_{ag} + \rho_{cp}\bar{\varepsilon}_{cp} \end{aligned} \tag{29}$$

where, $\bar{\sigma}_o$, $\bar{\sigma}_{ag}$ and $\bar{\sigma}_{cp}$ are the mean volumetric stresses on concrete, aggregate and cement paste, respectively, and $\bar{\varepsilon}_o$, $\bar{\varepsilon}_{ag}$ and $\bar{\varepsilon}_{cp}$ are the mean volumetric strains, ρ_{ag} and ρ_{cp} are the volume fractions of aggregate and cement paste, respectively. As the aggregate phase is assumed elastic, we have,

$$\bar{\varepsilon}_{ag} = \frac{1}{3K_{ag}}\bar{\sigma}_{ag}\,,\quad \bar{\varepsilon}_{cp} = f(\bar{\sigma}_{cp})\,, \tag{30}$$

where K_{ag} is the volumetric stiffness of aggregate.

Here, let us consider the local equilibrium and compatibility between two elements. If the cement paste matrix be a perfect liquid losing resistance to the shear deformation, we have $\bar{\sigma}_{ag} = \bar{\sigma}_{cp}$, where the shear stiffness of cement paste becomes zero. This system corresponds to Maxwell chain idealization. If the shear stiffness, G_{cp}, is infinitely large on the contrary, it brings no change of geometrical shape and results in $\bar{\varepsilon}_{ag} = \bar{\varepsilon}_{cp}$. This system corresponds to so called Kelvin chain. As the reality is in between two extremes, the Lagragian method of linear summation is applied as,

$$\left(\frac{\bar{\sigma}_{ag} - \bar{\sigma}_{cp}}{G_{cp}}\right) + \left(\bar{\varepsilon}_{ag} - \bar{\varepsilon}_{cp}\right) = 0 \tag{31}$$

Under the deviatoric shear mode of deformation, shear stress is hardly transferred through the contact link network of aggregates except for pre-packed concrete, and rotational resistance of individual particles is no longer expected when cement paste matrix deforms in shear. Thus, the authors assume that the space averaged deviatoric stress and strain of cement paste in concrete coincides with those of overall concrete composite. Then, we have,

$$S_{ij} = f(e_{ij}) \tag{32}$$

where, S_{ij} and e_{ij} are the deviatoric stress and strain tensors for both cement paste and concrete composite. The function f for cement paste is formulated as below.

The structural growth of cement paste is rather complex. Upon contact with water, powder particles start to dissolve and reaction products start to form. Due to gradual solidification of hydration products, properties of paste matrix vary with time. Solidification theory (Bazant and Prasannan 1989) proved a potential way of taking this aging effect into consideration.

As shown in **Fig. 15** and **Fig. 16**, growth of cement paste is idealized by forming finite fictitious clusters. When a new cluster is formed onto the already formed assembly of old clusters, strain of the cluster is originated at the time of birth. Aging process is represented by solidification of new cluster afterwards. In order to set a criterion for cluster formation, a volume fractional function is introduced. This function is taken as the hydration ratio at a certain time t, $\psi(t)$. It is defined as a ratio of hydrated volume of cement powder, $V(t)$, to total volume of cement that is available for hydration, V_{cp}, as,

$$\psi(t) = V(t) / V_{cp} \tag{33}$$

The structure of cement paste at any time is represented using the number of clusters already solidified at that time. According to hydration degree, numbers of clusters, N, at a certain time can be determined and when the hydration increment reaches a certain value a new cluster is developed and attached to the older ones. As these clusters share bearing stresses carried by the cement paste, we introduce an infinitesimal stress in each cluster, S_{cp}. When a new cluster is formed, these infinitesimal stresses are redistributed among the clusters. It also means that the stress condition in a certain cluster is a function of both current time and the location of this cluster or the time when this cluster was born.

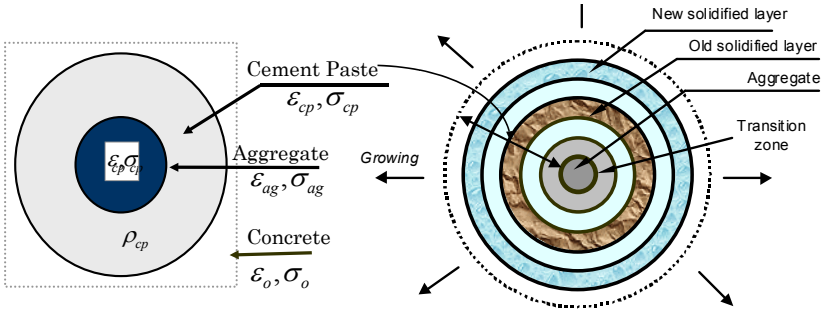

Fig. 15 Two-phase modeling of concrete composite – elastic suspension and nonlinear matrix –

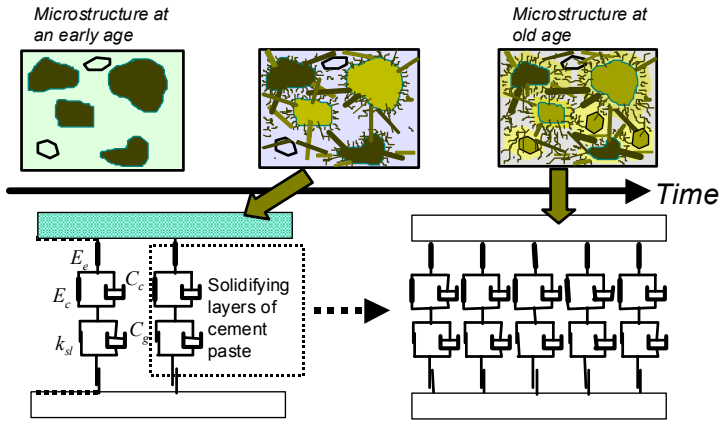

Fig. 16 Aging effect by solidified elasto-plastic assembly with different stress/strain histories.

Let S_{cp}=S_{cp} (t, t') denotes the average stress in a general cluster, where t is the current time and t' is the time when this cluster is solidified. Total volumetric stress in cement paste at a certain time is the summation of average stresses in all clusters activated at that time and strain in cement paste is equal to the one induced in each cluster. Solidification concept of cement paste cluster regarding growth of microstructure yields,

$$\bar{\sigma}_{cp}(t) = \int_{t'=0}^{t} S_{cp}(t',t)d\psi(t'),\ S_{ij}(t) = \int_{t'=0}^{t} S_{ij}(t',t)d\psi(t') \tag{34}$$

where, $S_{cp}(t', t)$ is the mean volumetric stress acting on a certain cluster, t' is the time when this cluster formed, t is the current time, ψ is the hydration degree, $S_{ij}(t', t)$ is the deviatoric stress tensor acting on the cluster concerned. When new cluster is formed, specific cluster stress is null. Then, we have S_{cp} (t, t)= 0 and S_{ij} (t, t)= 0.

3.7.2 Modeling of solidifying cement paste cluster

The solidifying mechanical unit as shown in **Fig. 16** is thought to be associated with CSH gel grains. Thus, the time-dependent deformation rooted in moisture in gel and interlayer pores should be taken into account in each individual solidifying component. The assembly of solidifying components corresponds to cement paste. Here, the moisture existing in capillary pores between gel grains has to be taken into account in the model, too. The authors simply assume two fictitious time-dependent deformational components rooted in both interlayer/gel pores and capillary one as shown in **Fig. 17** (Mabrouk et al. 1998 and 2000). Moisture transport actually takes place into the capillary and gel pores. Under severe drying, interlayer water starts to be in motion. Thus, moisture transport related to each of these pores categories can be correlated to a certain aspect of the creep behaviors (Glucklich 1959, Neville 1959).

The rate of flow of capillary water is comparatively high and easily reversible. Thus, moisture transport within capillary pores can be assumed as a cause of short-term creep at earlier ages. This creep rate drops steeply with time and is highly related to the hydration process. Moisture transport within gel pores is thought to be slow and prolonged in nature. Kinematics of gel water can be reversible up to a certain limit. It can be assumed as a cause of long-term creep and is responsible for the main part of the unrecoverable creep. Moisture migration within interlayer pores can be assumed to drive creep under severe conditions. This creep is highly irreversible accompanying so called disjoining pressure.

In order to reflect three aspects of creep behaviors, a simple rheological model for each cluster component is assumed as shown in **Fig. 17**. The same model is adopted for both volumetric and deviatoric components. Here, the volumetric component is discussed in detail. Total strain of each solidifying cluster is decomposed into instantaneous elastic strain ε_e, visco-elastic strain ε_c, visco-plastic strain ε_g and instantaneous plastic strain ε_l.

$$\varepsilon'_{cp} = \varepsilon_e + \varepsilon_c + \varepsilon_g + \varepsilon_l \tag{35}$$

where, ε_{cp}' is the volumetric strain in a general layer.

It should be noted here that ε_{cp}' is the strain induced in an individual cluster after its solidification. As the clusters are assumed to join together, these strains should be common to corresponding volumetric strain in cement paste. However, clusters solidify at zero stress state. Thus, as given by Eq. 36, this strain at a certain time, t, is defined as the difference between the strain of cement paste at time, t, and the strain of cement paste at the time when the cluster solidified, t'.

$$\varepsilon'_{cp}(t) = \varepsilon_{cp}(t) - \varepsilon_{cp}(t') \tag{36}$$

(1) Instantaneous elasticity

The elastic spring of solidifying cluster represents the instantaneous deformation and assumed to be perfect elasticity as,

$$S_{cp} = E_e \varepsilon_e \tag{37}$$

where, S_{cp} is the volumetric stress in a cluster, E_e is the stiffness and ε_e is the instantaneous elastic strain. The elastic stiffness of the component is calculated so that summation of stiffness over all solidified clusters at a certain time is equal to that of cement paste.

(2) Visco-elasticity

The visco-elasticity represents delayed recoverable deformation. This is thought associated with rather larger sizes of micro-pores like capillaries and it macroscopically represents the short-term creep behaviors as,

$$S_{cp} = E_c \cdot \varepsilon_c + C_c \frac{d\varepsilon_c}{dt} \tag{38}$$

where, E_c is the stiffness and assumed $2.0{*}E_e$. ε_c is visco-elastic strain and C_c is defined as a constant of the dashpot fluidity related to moisture kept in capillary pores. The dashpot is related to condensed water motion through capillary pores associated with thermo hydro-physical requirements, and the following assumption is presented as,

$$C_c = a \cdot f(S_{cap}) \cdot \eta \cdot \phi_{cap}^{-1} \tag{39}$$

where, a is a constant, ϕ_{cap} is capillary porosity of the paste, S_{cap} is saturation of capillary pores, η is average viscosity of condensed water in micro pores. Function, f, can be defined as shown in **Fig. 17**.

(3) Visco-Plasticity

The visco-plasticity represents the time-dependent unrecoverable deformation mainly rooted in moisture kinematics in gel and interlayer pores. First, let us consider a simple case where applied stress on a cluster is constant. Plastic strain increases with time and finally may reach convergence denoted by ε_{glim}. Rate of plasticity to convergence is deemed influenced by the moisture residing inside gel pores. Dry empty pores shall bring rapid convergence of plasticity and wet moisture occupying pores may retard plasticity due to seepage.

As a matter of fact, possible converged plasticity is affected by applied stress level. At the same time, moisture in gel pores should be considered, because condensed and adsorbed water occupy micro-pore space. Here, the authors assume the simplest formula under generic stress paths, i.e., linear viscosity in terms of moisture mass in gel pores, linear converging strain in terms of applied stress, linear rate of plasticity in terms of updated plastic strain as follows.

$$\frac{d\varepsilon_g}{dt} = (\varepsilon_{g\lim} - \varepsilon_g)/C_g,\ C_g = d \cdot f(S_{gel}) \cdot \eta \cdot \phi_{gel} \tag{40}$$

$$\begin{aligned} \varepsilon_{g\lim} &= f_1(S_{cp}) \cdot f_2(S_{gel}) \\ f_1 &= S_{cp}/E_g,\ E_g = E_e/4 \\ f_2 &= \exp(-a \cdot S_{gel}) \end{aligned} \tag{41}$$

where, S_{gel}: saturation of gel pores, d: constant, ϕ_{gel}: gel porosity of paste related to this arbitrary cluster, η: viscosity of micro pore water.

(4) Instantaneous plasticity

Motion of interlayer moisture or some of gel water causes instantaneous volume change since the size of the pores is close to that of water molecule. The instantaneous plasticity related to ambient condition is assumed associated with saturation of interlayer pore as,

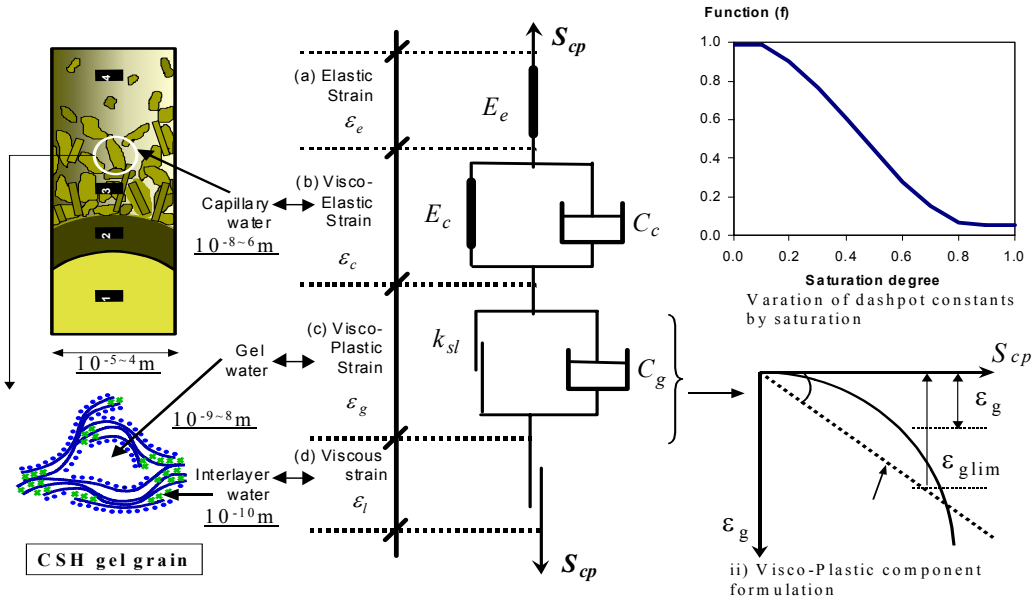

Fig. 17 Modeling of solidifying cluster of cement hydrate.

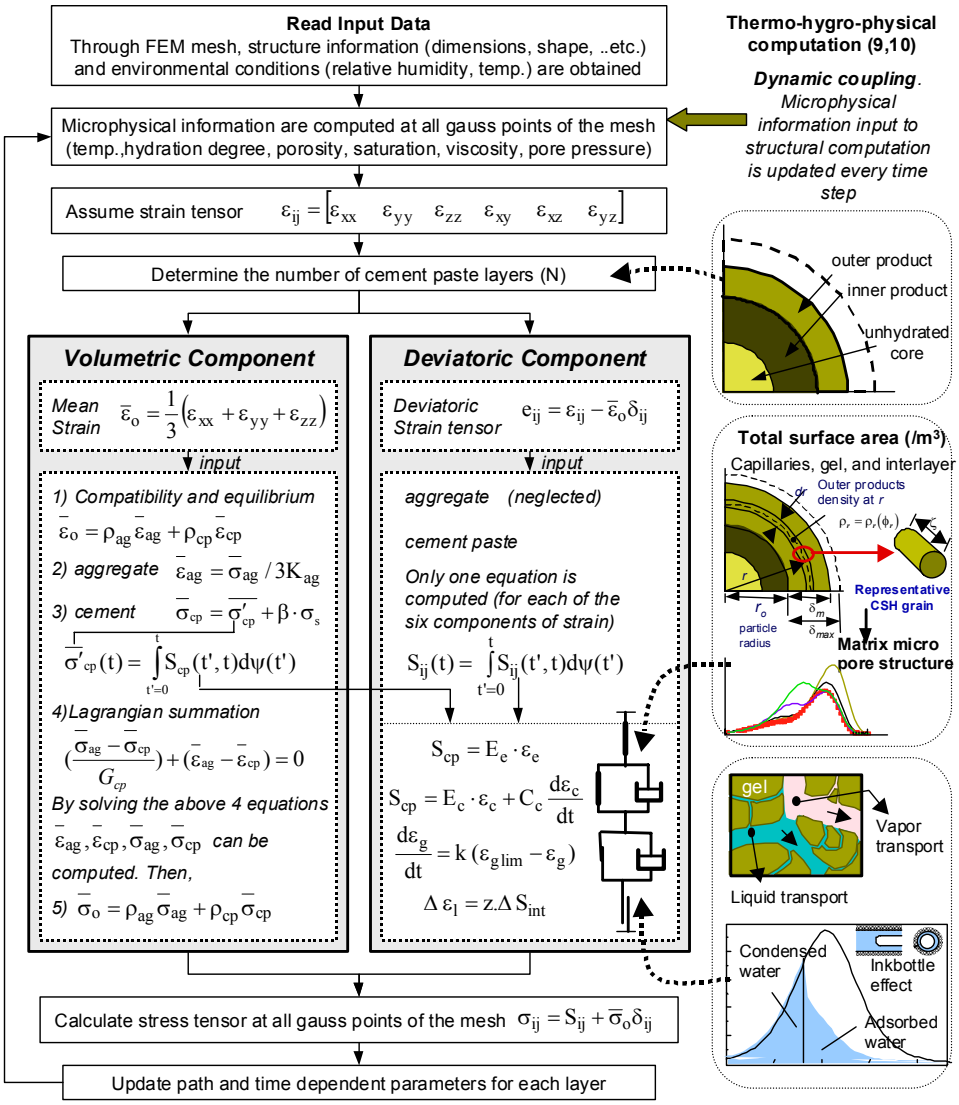

Fig. 18 System dynamics and flow of computation based on particle dispersion and solidification.

$$\Delta \varepsilon_l = z \cdot \Delta S_{int} \tag{42}$$

where, ε_l : moisture related instantaneous strain, z: constant, and S_{int} : saturation of interlayer. This component is not in motion under usual ambient conditions. But, it may work under very dry situations and/or higher temperatures. Entire set of assumed material functions and constants are summarized in **Fig. 18**.

3.7.3 Coupling of skeleton stresses and pore water pressure

In this section, effect of micro-pore pressure on deformation of cement paste solid is introduced. Pressure drop of condensed water in micro-pores is equilibrated with capillary surface tension acting between liquid and gas phases, and it is assumed as one of causes of shrinkage (Shimomura and Maekawa 1997). Since surface tension developing in micro-pores is isotropic, only the volumetric mode of deformation is targeted. Similar to Biot's theorem of two-phase continuum, volumetric stress of cement paste is idealized as carried by both skeleton solid and pore pressure (Maekawa et al. 1999, Ishida et al. 1999a and 1999b) as,

$$\bar{\sigma}_{cp} = \overline{\sigma'_{cp}} + \beta \cdot \sigma_s \tag{43}$$

where, σ'_{cp} is volumetric stress by cement paste skeleton and σ_s is pore-water pressure drop. Factor β indicates effectiveness to represent the volume fraction where moisture can act. If the whole space is occupied by water continuum, it is unity as Biot's theory reveals.

Pore water pressure can be evaluated by Kelvin's formula and factor β is estimated in use of micro-pore water information as,

$$\sigma_s = -\frac{2.\gamma}{r_s} = -\frac{\rho.R.T}{M}\ln h \,,\beta = \frac{\phi_{cap}\cdot S_{cap} + \phi_{gel}\cdot S_{gel}}{\phi_{cap} + \phi_{gel}} \quad (44)$$

where, γ: surface tension of condensed water, r_s: pore radius at which the interface is created, R: universal gas constant, T: absolute temperature of vapor-liquid system, M: molecular mass of the water, h: relative humidity i.e. the ratio of the vapor pressure to the saturated vapor pressure.

This coupling is a key to integrate thermo-hydro dynamics and deformational solid mechanics of concrete composite, and effect of moisture on deformation is inherently taken into account. Moisture loss may occur due to cement hydration and/or moisture migration invoked by drying climates. The volumetric change caused by both can be systematically included in the constitutive modeling of multi-scale. Thus, there is no need to assume specific drying/autogenous shrinkage, and basic/drying creep. Mathematical formula based on the basic hypothesis -particle dispersion of aggregates and solidification of cement- are summarized in **Fig. 18**.

3.7.4 Simulation and verification

In this section, the framework involving both the computation of thermo-hydro-physical information and the simulation of the structure behavior is presented. **Fig. 19** shows a summary of the model parameters and their computation. Creep and shrinkage are targets of experimental verification and comparison with available experimental data is conducted.

Firstly, two pure cement paste specimens (S1, S2) of young age are studied as shown in **Fig. 20**. Here, aging process represented by solidification of clusters, creep at young age as represented by the visco-elastic part and coupling with pore water pressure for computation of shrinkage are the main parts affecting the results. From the figure, good agreement can be obtained between analysis and experiment in case of drying shrinkage, S1, while the results are rather overestimated in the case of loaded specimen, S2. Concrete based verification follows the verification as S3 in **Fig. 21**. Reasonable agreement is seen. Here, coupling between the skeleton stress of cement paste and the pore water pressure is a main concern of verification.

In **Fig. 22**, two concrete cylinder specimens, S4 and S5 (Neville 1959), are studied in terms of normalized creep ratio per unit stress. Case S5 shows creep under sealed conditions at the age of 28 days. In this case, moisture loss does not occur and aging is almost completed. In case of S4, drying is allowed. Here the effect of the visco-plastic component becomes more apparent and creep is increased. Comparison between experiment and analysis are reasonable. However, irreversible deformation by drying is underestimated.

In addition, two cement paste beams, S6 and S7 (Glucklich 1959), were studied as shown in **Fig. 23**. These cases represent a simple verification on the structure level. Once again reasonable results are obtained. It can also be shown that the loading-unloading pattern in the case of S7 can be well represented. This part is mainly linked to the slider and dashpot of the visco-plastic component.

Combination of autogenous and drying shrinkage is studied as below. Drying accerlates dessication insde micro-pores together with cement hydration. At the same time, moisture loss close to surfaces may retard hydration at early age accompanying corser solids and eacy loss of moisture. Computation seems acceptable as shown in **Fig. 24**. As the micro-climate is automatically computed in this holistic approach, relative humidity in pores can be shown, too. Self-dessication of W/C=30% is more severe.

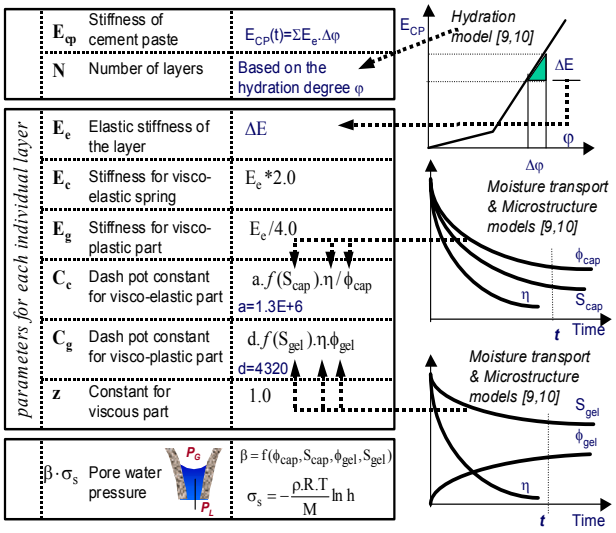

Fig. 19 Model parameters and their computations.

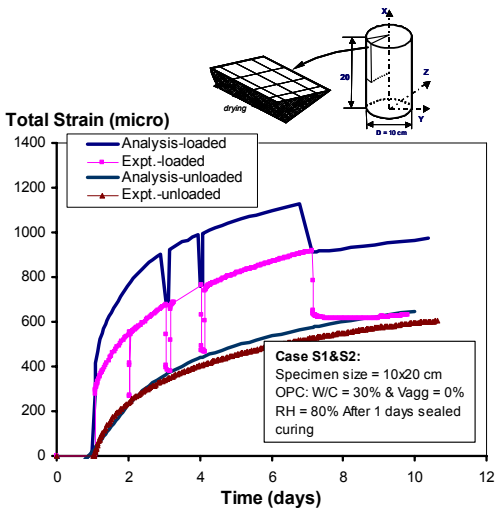

Fig. 20 Creep/shrinkage simulation and verification.

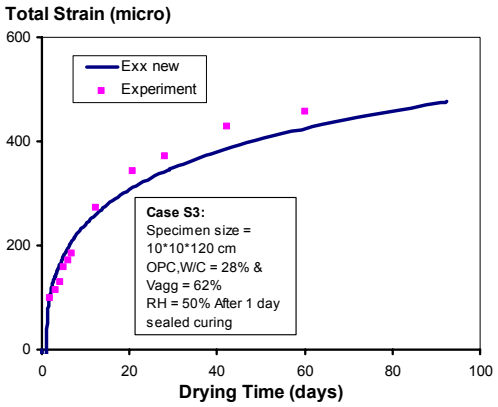

Fig. 21 Free shrinkage simulation and verification.

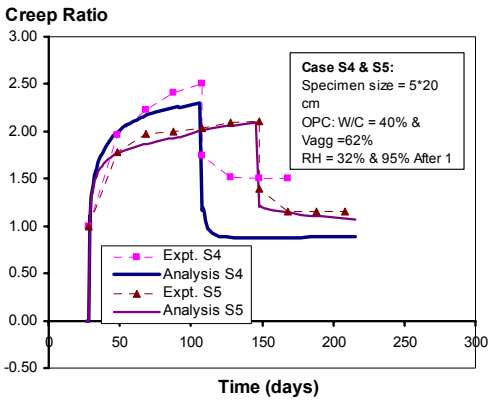

Fig. 22 Basic and drying creep simulation.

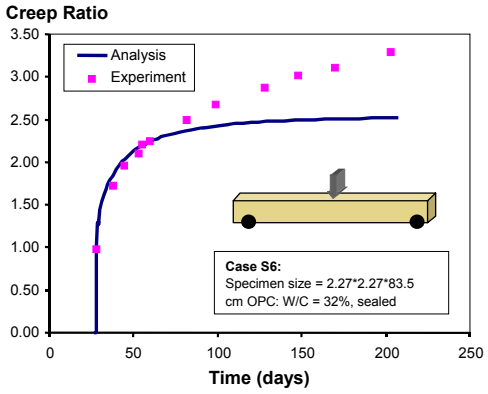

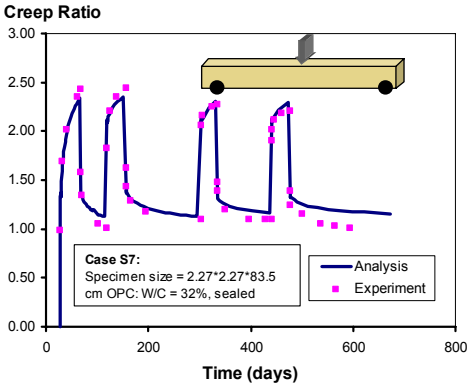

Fig. 23 Simulation of time-dependent deflection of beams under sealed condition.

3.8 Model of Macro-Cracks in Concrete – 10^{-3} ~10^{-0} *m Scale* -

For simulating structural behaviors expressed by displacement, deformation, stresses and macro-defects of materials in view of continuum plasticity, fracturing and cracking, well established continuum mechanics is available in multi-scale modeling. Compatibility condition, equilibrium and constitutive modeling of material mechanics are the basis and spatial averaging of overall defects in control volume of meso-scale finite element is incorporated into the constitutive model of quasi continuum. Here, the size of referential volume is $10^{-3} \sim 10^{-1}$ m order. The authors adopted a 3D finite element computer code of nonlinear structural dynamics (Maekawa et al. 2003).

This frame of structural mechanics has an inter-link with thermo-hydro physics in terms of mechanical performances of materials through the constitutive modeling in both space and time (**Fig. 2**). The instantaneous stiffness, short-term strengths of concrete in tension and compression, free volumetric contraction rooted in coupled water loss and self-desiccation caused by varying pore sizes are considered in the creep constitutive modeling of liner convolution integral. The volumetric change invoked by the hydration in progress and water loss is physically tied with surface tension force developing inside the micro-capillary pores. The micro-pore size distribution and moisture balance of thermo dynamic equilibrium are given from the code *DuCOM* at each time step as discussed in previous chapters.

Cracking is the most important damage index associated with mass transport inside the targeted structures. Cracks are assumed normal to the maximum principal stress direction in 3D extent when the tensile principal stress exceeds the tensile strength of concrete. After crack initiation, tension softening on progressive crack planes is taken into account in the form of fracture mechanics. In the reinforced concrete zone, in which bond stress transfer is expected being effective, tension stiffness model is brought together. Since the external load level, with which the environmental action be coupled in design, is rather lower than ultimate limit states, compression induced damage accompanying dispersed micro cracking is disregarded. **Fig. 25** shows the overall frame of constitutive modeling of macro-scale REV including cracks. This macroscopic modeling, which can be directly used for behavioral simulation of entire structures, has the mutual link with nanometer-scale structures as shown in **Fig. 1**.

In the case where mechanical actions on structures are

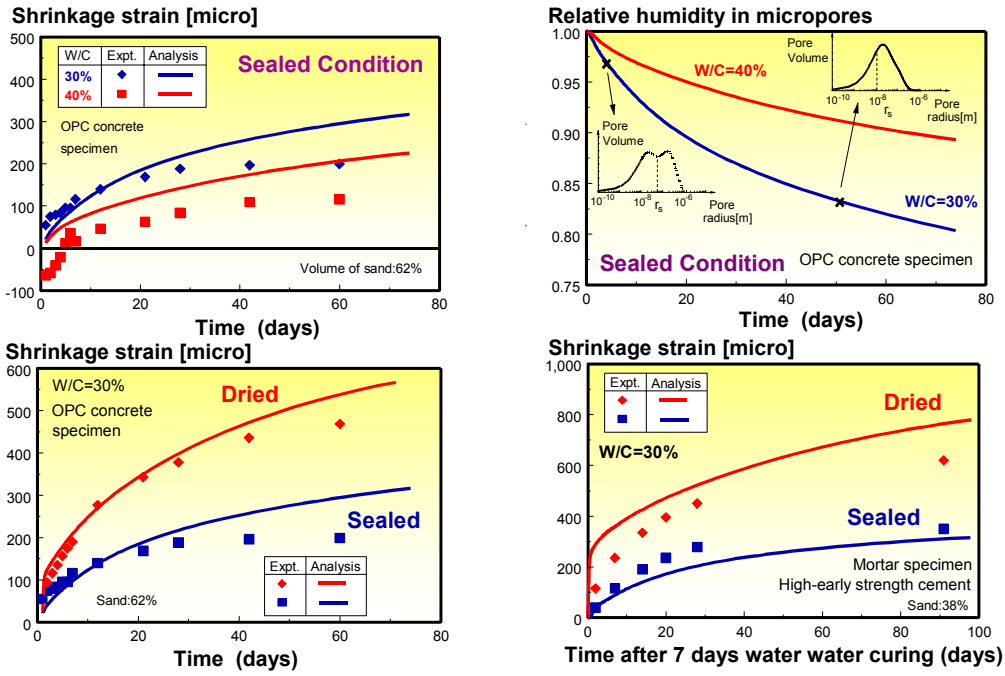

Fig. 24 Volume change simulation under coupled autogenous and drying shrinkage and internal states.

dominant, multi-directional cracks intersect orthogonally, because the principal stress hardly rotates in nature. In the case where both mechanical and ambient weather actions are applied to concrete structures, however, principal stress axes can drastically rotate and non-orthogonal cracking easily takes place in the REV domain. As highly nonlinear interaction between multi-directional cracking is witnessed, the rotating crack model or single directional smeared crack approach is hardly used for structural damage analysis under coupled loads and ambient conditions.

In this study, multi-directional fixed crack modeling of the RC domain is applied. This modeling was originally developed for reversed cyclic finite element analysis for three-dimensional RC under arbitral ground motions. As a matter of fact, multi-directional forces may cause non-orthogonal cracks in nature. Here, the active crack method is utilized for simplifying numerical processes with reasonable accuracy for practice, and currently used for seismic performance assessment of underground RC and energy facilities.

In this scheme of controlling multi-directional cracking, the most active crack which dominates the nonlinearity of the whole domain is selected and the rest of the cracks is assumed dormant with no evolution of shear transfer plasticity and fracturing as illustrated in **Fig. 26**.

4. Numerical Simulations

4.1 Re-hydration and Varying Permeation

It is experienced in laboratories that tested permeation of water through lower water to cement ratio concrete/mortar is time-dependent. Re-hydration and self-curing were reported for concrete with unhydrated cement. Prematurely cured concrete performance can be recovered by re-wetting. Thus, it will be agreed that tested permeability of cementitious composites is not the characteristic constant of material performance. The authors conducted long-term simulation of coupled moisture migration, re-hydration and reforming of micro-pores as shown in **Fig. 27**.

It is clearly observed that micro-pore spaces of larger water to cement ratio concrete are entirely occupied by water within a shorter period except the extreme end exposed to dry air. In contrast, micro-pores of low water to cement concrete are hardly filled with moisture and it takes many years for stability in computation. As severe self-desiccation occurs inside the core of concrete, moisture intake is made from the drying boundary. At the other boundary attached to condensed water, re-started hydration makes pores denser and condensed water migration is strongly blocked and vapor diffusivity chiefly conveys moisture inside the analysis domain. Only with short-term tested permeation, it is difficult to evaluate the concrete performance against moisture leakage for low water to cement ratio concrete. In this analysis, the calcium leaching was not coupled for simplicity.

4.2 Chloride Transport into Concrete Under Cyclic Drying-Wetting

Using the proposed method, transport of chloride ion under alternate drying wetting conditions is presented. For verification, experimental data by Maruya et al. (1998) is used. The size of mortar specimens is 5×5×10

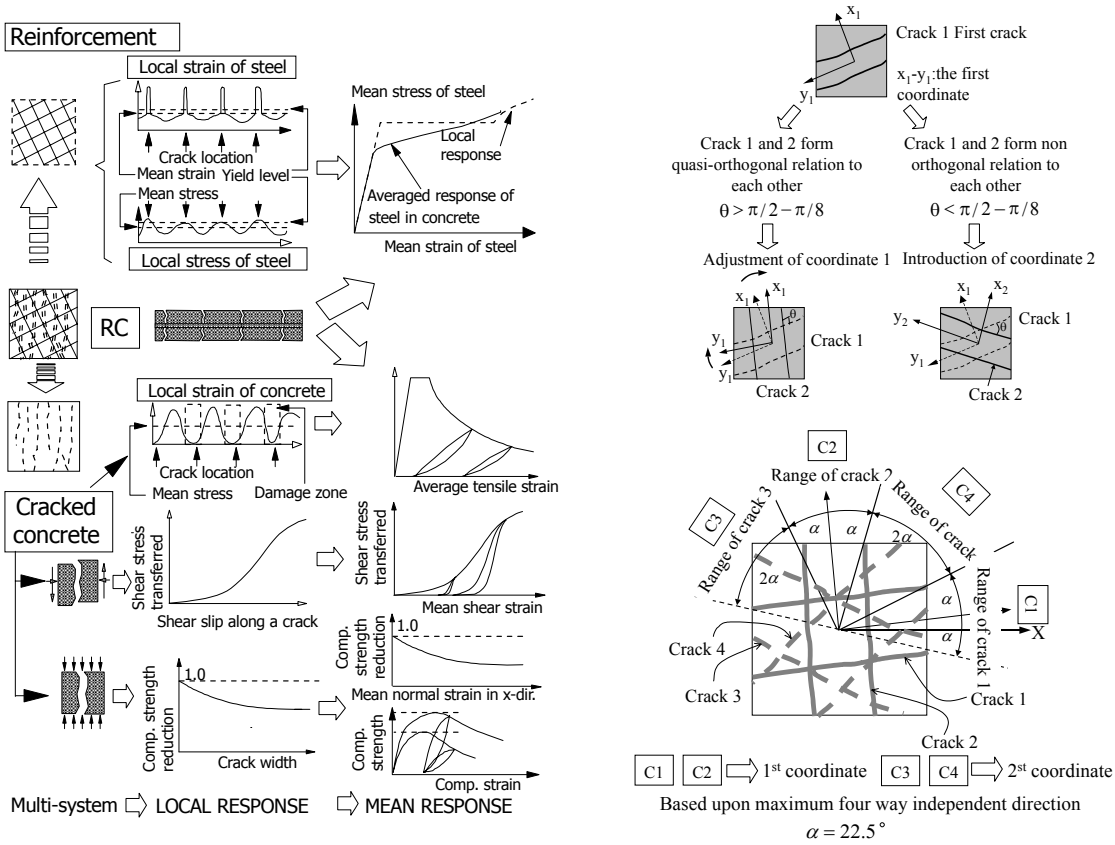

Fig. 25 Macroscopic modeling of reinforced concrete with cracking: REV size is about 10^{-3}~10^{-0}m.

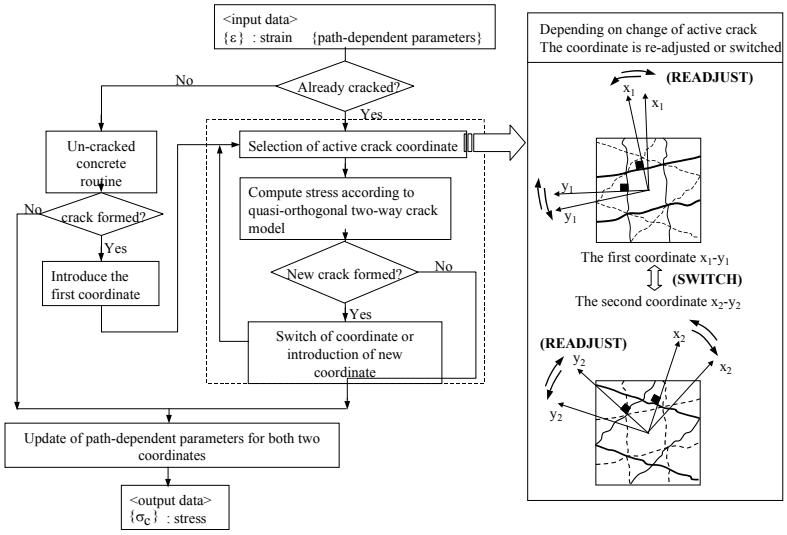

Fig. 26 Active and dormant crack scheme for multi-directional cracking model.

[cm] and the water to powder ratio is 50%. After 28 days of sealed curing, the specimens were exposed to cyclic alternate drying (7 days) and wetting (7 days) cycles. The drying condition was 60%RH, whereas the wetting was exposed to a chloride solution of 0.51 [mol/l] at 20ºC. In FEM analysis, mix proportions and chemical compositions of cements are given. The curing and exposure conditions are also defined as boundary conditions for the target structures. All of these input values correspond to the experimental conditions. **Fig. 28** shows the distribution of free and bound chlorides from the surface of exposure. Two cases are compared; one considering only diffusive movement and the other including the advective transport due to the bulk movement of pore water as

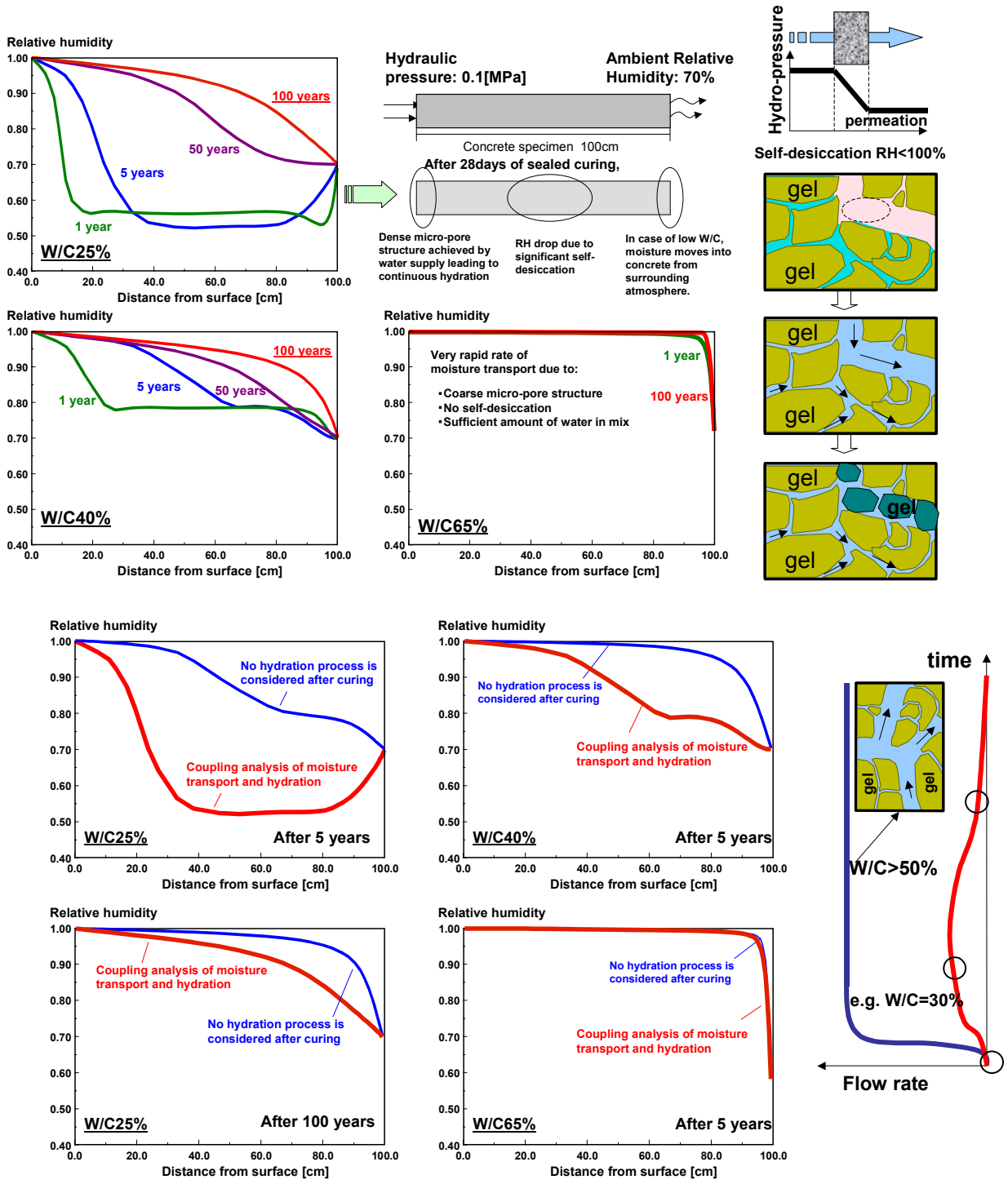

Fig. 27 Coupled moisture migration and transient evolution of micro-pore structures for low W/C.

well as the diffusion process. The distribution of bound and free chlorides can be reasonably simulated with advective transport due to the rapid suction of pore water under the wetting phase.

4.3 Carbonation Phenomena in Concrete

In this section, computations were performed to predict the progress of carbonation for different CO_2 concentrations and water to cement ratio. The amount of $Ca(OH)_2$ existing in cementitious materials can be obtained by the multi-component hydration model as (Kishi and Maekawa, 1996 and 1997),

$$\begin{aligned} 2C_3S + 6H &\rightarrow C_3S_2H_3 + 3Ca(OH)_2 \\ 2C_2S + 4H &\rightarrow C_3S_2H_3 + Ca(OH)_2 \\ C_4AF + 2Ca(OH)_2 + 10H &\rightarrow C_3AH_6 \end{aligned} \quad (45)$$

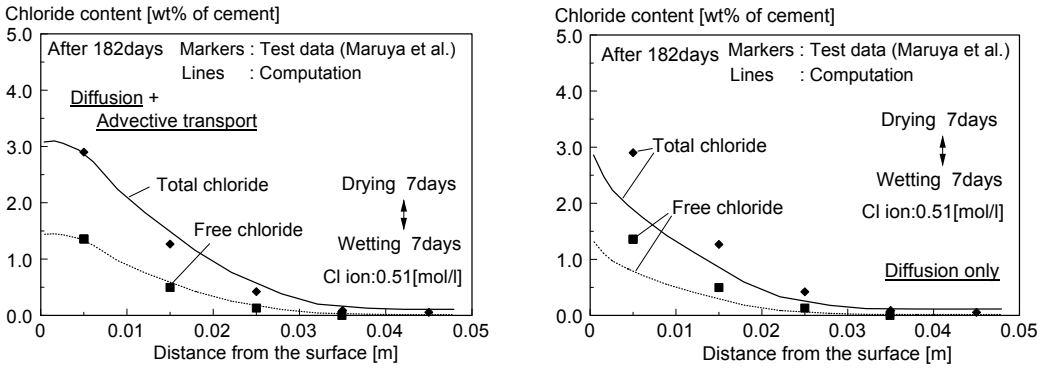

Fig. 28 Chloride content profile in concrete exposed to cyclic drying wetting and drying.

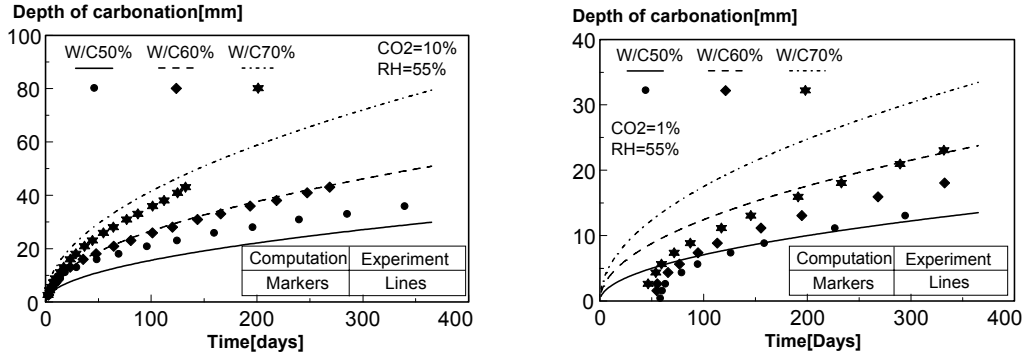

Fig. 29 Carbonation phenomena for different CO_2 concentrations and water-to-cement ratio.

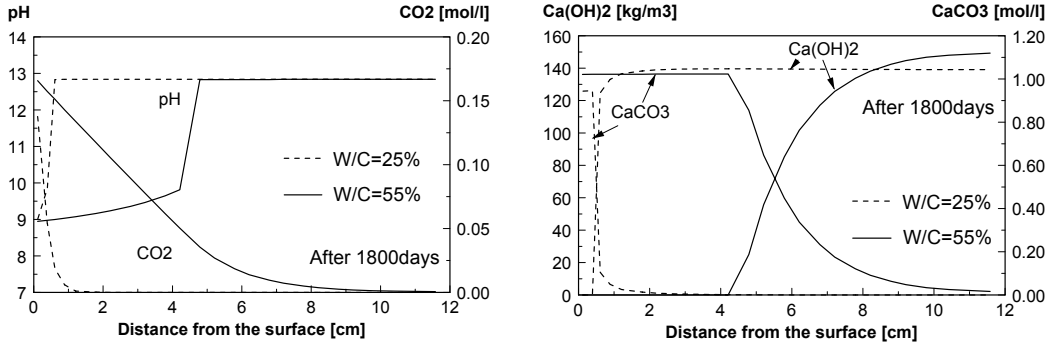

Fig. 30 Distribution of pH, calcium hydroxide, and calcium carbonate under the action of carbonic acid.

For verification, the experimental data done by Uomoto et al. (1993) were used. **Figure 29** shows the comparison of analytical results and empirical formula that was regressed with the *square root t equation*. Similar to the previous case, all of the input values in the analysis corresponded to the experimental conditions. Analytical results show the relationship between the depth of concrete in which pH in pore water becomes less than 10.0 and exposed time. The simulations can roughly predict the progress of carbonation for different CO_2 concentrations and water to powder ratios.

Fig. 30 shows the distribution of pH in pore water, CO_2, calcium hydroxide, and calcium carbonate inside concrete, exposed to the CO_2 concentration of 3%. Two different water to powder ratio, W/C=25% and 50%, were analyzed. It can be shown that higher resistance for the carbonic acid action is achieved in the case of a low W/C.

4.4 Coupled Carbonation and Chloride Induced Corrosion

Attention is directed to steel corrosion in concrete due to the simultaneous attack of chloride ions and carbon dioxide. Provided that concrete is totally submerged, corrosion rate is small to a great extent due to the much lower supply of oxygen. Thus, drying is also coupled. Interaction of chloride and CO_2 sub-phases is modeled such that bound versus free chloride equilibrium is influenced by pH of pore solution. The authors assume pH sensitivity as shown in **Fig. 31** from some literature and densification of micro-pores caused by carbonation is simply expressed by the reduction factor of porosity. This

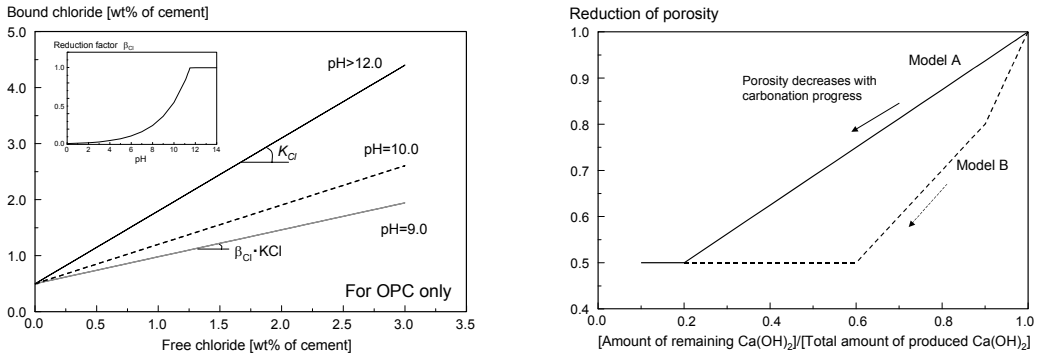

Fig. 31 Release of bound chloride and re-densification of pores by carbonation.

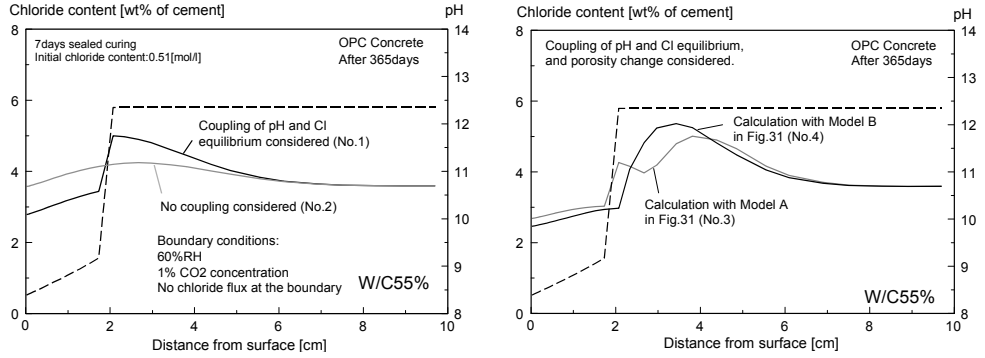

Fig. 32 Computation of total chloride contents under coupled drying, carbonation and chloride penetration.

is to express the replacement of $Ca(OH)_2$ and calcite.

Figure 32 solely shows simulation. The carbonated zone close to the surface shows evidence of smaller total chloride due to released bound chloride by carbonation and loss of moisture by drying, but dissolved chloride ion is concentrated in the pore solution. Around the carbonation front, a couple of peaks of total chloride are formed. Here, the free chloride is released from formerly bound chloride. Since the carbonation brings densification of pores, chloride ion penetration is also held back and twin peaks can be formed just close to the carbonation front. In the future, detailed discussion will be beneficial in this regard.

For life-span assessment, concrete members with different water to powder ratios, W/C=40, 50, 60%, with only one face exposed to the environment were considered. The stage where concrete cracking occurs was defined as a limit state with respect to the steel corrosion. The progressive period until the initiation of longitudinal cracking was estimated by the equation proposed by Yokozeki et al. (1997), which is a function of cover depth. **Fig. 33** shows relationships between cover depth and structural age until cracking due to corrosion obtained by the proposed thermo-hydro system. It can be seen that the concrete closer to the exposure surface will show an early sign of corrosion induced cracking, and low W/C concrete has the higher resistance against corrosion.

4.5 Moisture Distribution in Cracked Concrete

In this section, in order to show the possibility of a unification of structure and durability design, a simple simulation was conducted by using the proposed parallel computational system. It has been reported that there should be a close relationship between moisture conductivity and the damage level of cracked concrete; that is, moisture conductivity should be dependent on the crack width or the continuity of each crack. The proposed system, in which information is shared between the thermo-hydro and structural mechanics processes, is able to describe this behavior quantitatively by considering the inter-relationship between moisture conductivity and cracking properties. For representing the acceleration of drying out due to cracking, the following model proposed by Shimomura (1998) was used in this analysis.

$$J_w = \begin{cases} J_V + J_L & \textit{before cracking} \\ J_V + J_L + J_V^{cr} + J_L^{cr} & \textit{after cracking} \end{cases} \tag{46}$$

where, J_w is the total mass flux of water in concrete, J_V and J_L are the mass flux of vapor and liquid in non-damaged concrete respectively, and J_V^{cr} and J_L^{cr} are the mass flux of vapor and liquid water through cracks. In this simulation, only J_V^{cr} is taken into account for the first approximation, since diffusion of vapor would be predominant when concrete are exposed to drying conditions. From the experimental study done by Nishi et al.

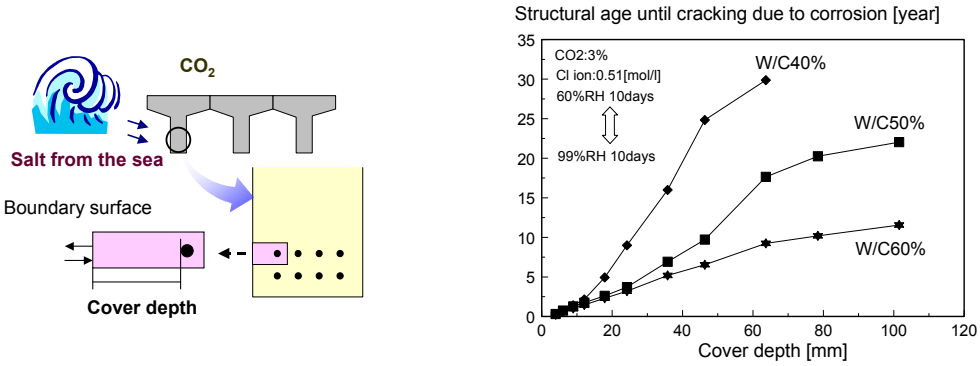

Fig. 33 Time till first sings of cracking due to corrosion for concrete exposed to CO_2 gas and salty water.

(1999), it has been confirmed that the flux J_V^{cr} can be expressed as,

$$J_V^{cr} = -\bar{\varepsilon}\rho_V D_a \nabla h \tag{47}$$

where, $\bar{\varepsilon}$: average strain of cracked concrete, which can be computed by COM3, ρ_V: density of vapor, D_a: vapor diffusivity in free atmosphere, h: relative humidity.

The target structure in this analysis was a concrete slab, which has 30% water to powder ratio using medium heat cement. Mesh layout and the restraint conditions used in this analysis are shown in **Fig. 34**. The volume of aggregate was 70%. After 3 days of sealed curing, the specimen was exposed to 50%RH. **Figure 34** shows the cracked elements, the distribution of moisture, and normalized tensile stress at each point from the boundary surface exposed to drying condition. Moisture distribution calculated without stress analysis is also shown in **Fig. 34**. As shown in the results, the crack occurs from the element near the surface, and the crack progresses internally with the progress of drying. It is also shown that the amount of moisture loss becomes large due to cracking.

4.6 Coupling of Shear and Axial Forces Invoked by Volume Change

When thermally induced cracks penetrate through a whole section, a diagonal shear crack may be arrested by pre-existing damage induced by heat and/or drying as shown in **Fig. 35**. The stiffness of the member is certainly reduced by the crack penetrating the entire section, but the shear capacity is, on the contrary, elevated since

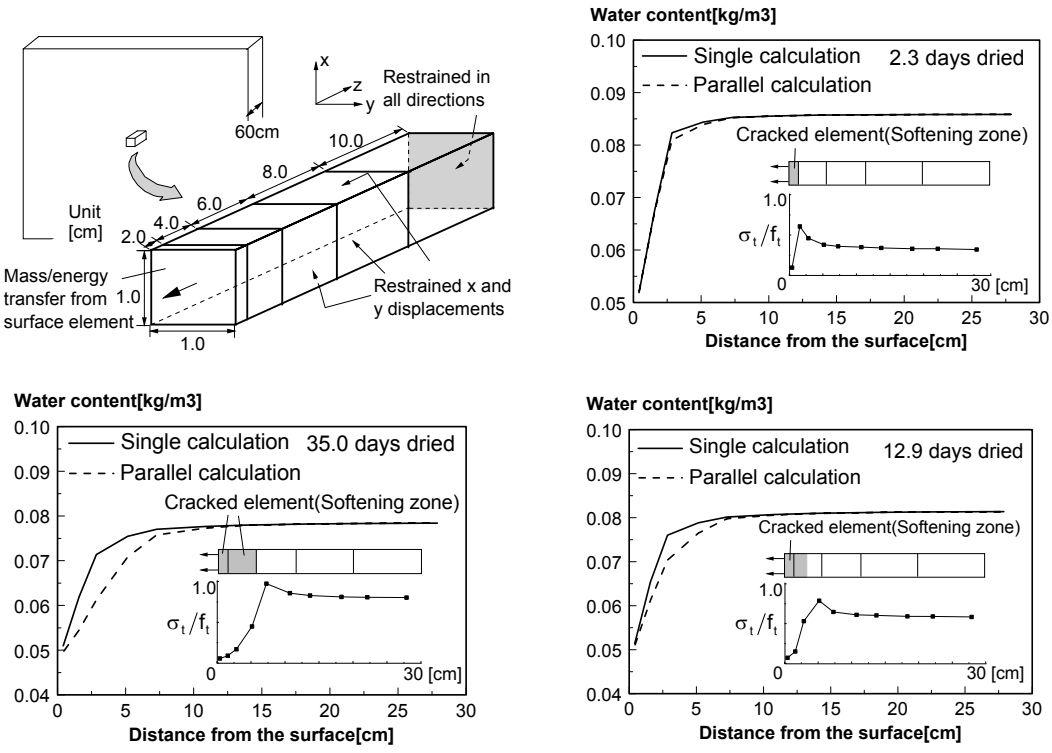

Fig. 34 Moisture and internal stress distribution in concrete exposed to drying condition.

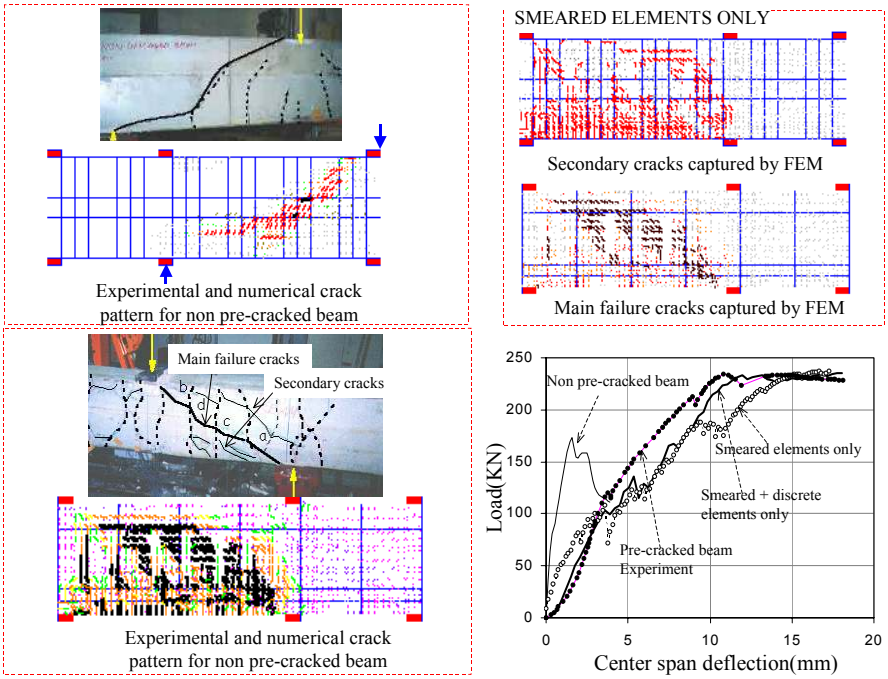

Fig. 35 Interaction of non-orthogonal cracking and safety performance simulation.

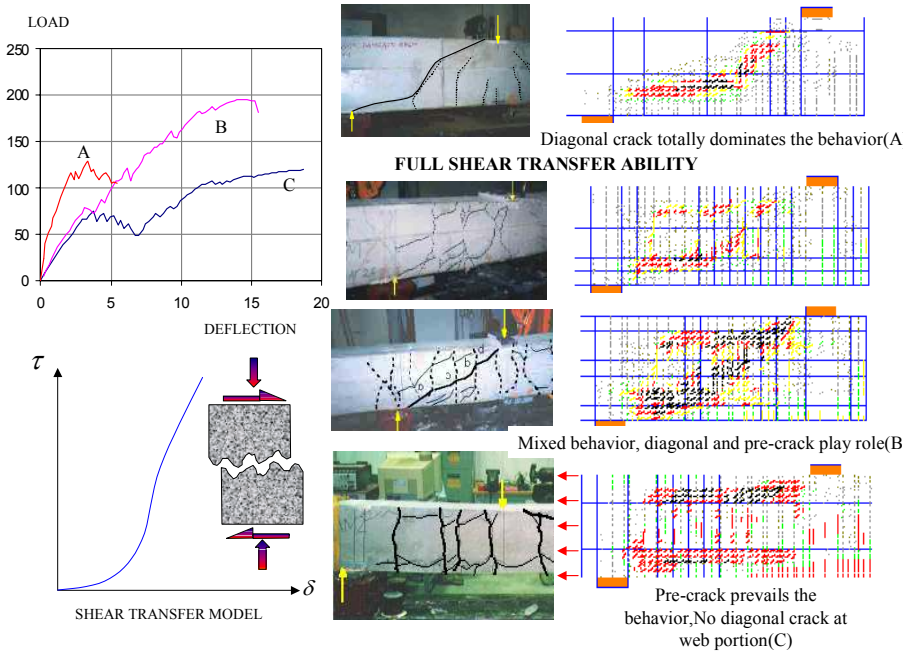

Fig. 36 Effect of pre-induced crack width on the shear capacity.

the shear crack propagation is retarded or has ceased. Non-orthogonal crack-to-crack interaction can be well simulated and the localization pattern of force-induced cracks is greatly affected by the damage level of pre-cracks in terms of average strain as shown in **Fig. 36**. This is attributed to shear transfer performance of concrete crack planes. Here, the contact density model for concrete rough cracks is applied. The shear transfer which causes principal stress rotation is one of crucial mechanics for coupled force-environmental actions.

4.7 Corrosion-Induced Cracking and Structural Capacity

Figure 37(a) shows the chloride ion penetration into the beam subjected to flexure. The bending cracks are distributed around the lower extreme fiber and the averaged

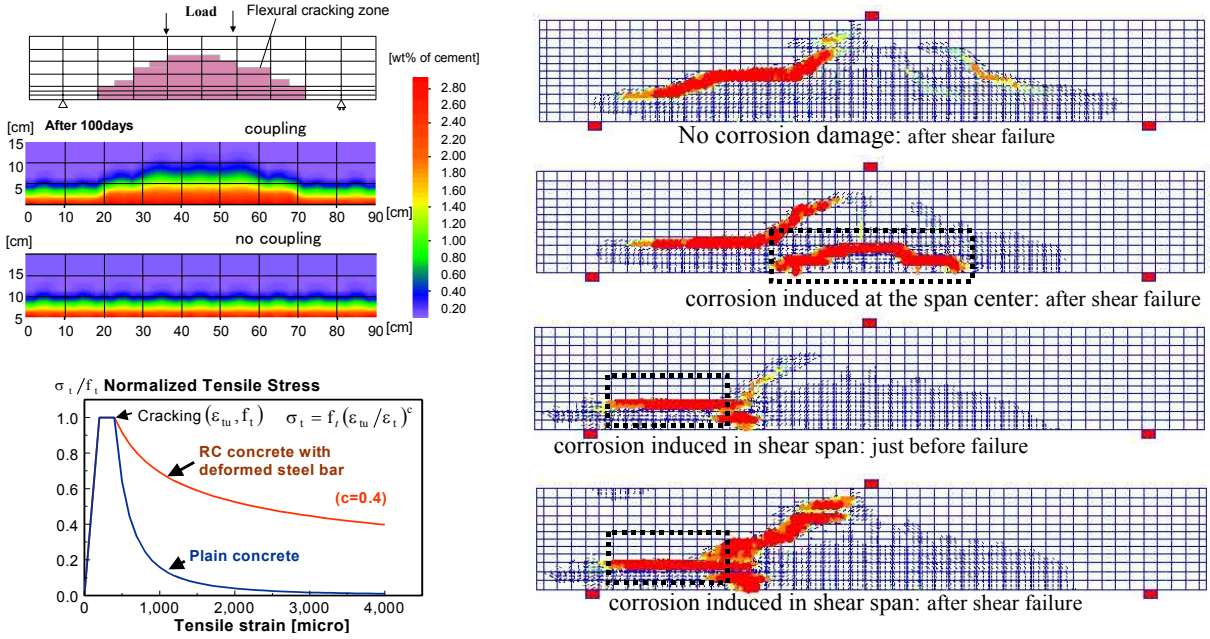

(a) Crack-diffusion interaction (b) Shear and corrosion crack interaction

Fig. 37 Corrosion induced cracking and remaining structural performance assessment.

tensile strain is transferred to a DuCOM sub-system. As the chloride ion diffusivity is formulated based upon both pore-structural characters (micro-information) and crack strain (macro-information) dependent on applied loads, the deep penetration is seen at the center span of the beam.

The cracking pattern of an RC beam subjected to shear and flexure is illustrated in **Fig. 37(b)**. As the shear capacity is less than the flexural one, a localized shear crack band can be seen after failure. Firstly, partial corrosion is numerically reproduced by concentrated chloride with longitudinal cracking and followed by load. Here, the stiffness of corroded substance treated as perfect elasticity is assumed 7GPa and its volume expansion rate is set 3 times. The tension-stiffness defined in finite elements with corroded steel is reduced to plain concrete softening since the bond is thought deteriorated.

If the corrosion induced cracking is located around the center span, no interaction of shear and flexural cracks is seen and shear capacity of the beam is computed unchanged. When it is placed around the shear span close to the support, diagonal shear crack joins this pre-cracking and early penetration of the diagonal crack is computed. Non-orthogonal cracking is the key of this analysis.

4.8 Time-Dependent Deflection of Beams under Drying

Two beams as shown in **Fig. 38** are discussed concerning the load-drying combination. Under pure drying with no external forces, no deflection takes place in nature as no curvature is developed. Under the sealed condition without moisture loss, creep deflection is caused by concrete creep in compression and tension. When two actions are simultaneously combined, time-dependency of deflection is significantly stepped up as shown in **Fig. 38**. This apparent nonlinearity is known as the Pikket effect and practically, the creep function is specified differently from basic creep. In multi-scale analysis, there is no need to change material functions under different ambient conditions.

The drying effect is explicitly considered as a moist boundary condition, and the pore-water pressure is computed in DuCOM. The self-equilibrated stress and deformation concurrently solved space by space and creep properties of skeleton stress and strain are evaluated with micro-damage if any.

5. Conclusions

Chemo-physical and mechanical modeling of concrete with greatly different scales of geometry was presented, and synthesized on a unified computational platform from which quantitative assessment of structural concrete performances may derive. Experimental verifications show its possibility as a holistic approach, while individual modeling of chemical-physical events is required to be enhanced in the future with continuous effort. Currently granted is a great deal of knowledge earned by the past development. At the same time, we face a difficulty to quantitatively extract consequential figures from them. The authors expect that the systematic framework on the knowledge-based technology will be extended efficiently and can be steadily taken over by engineers in charge.

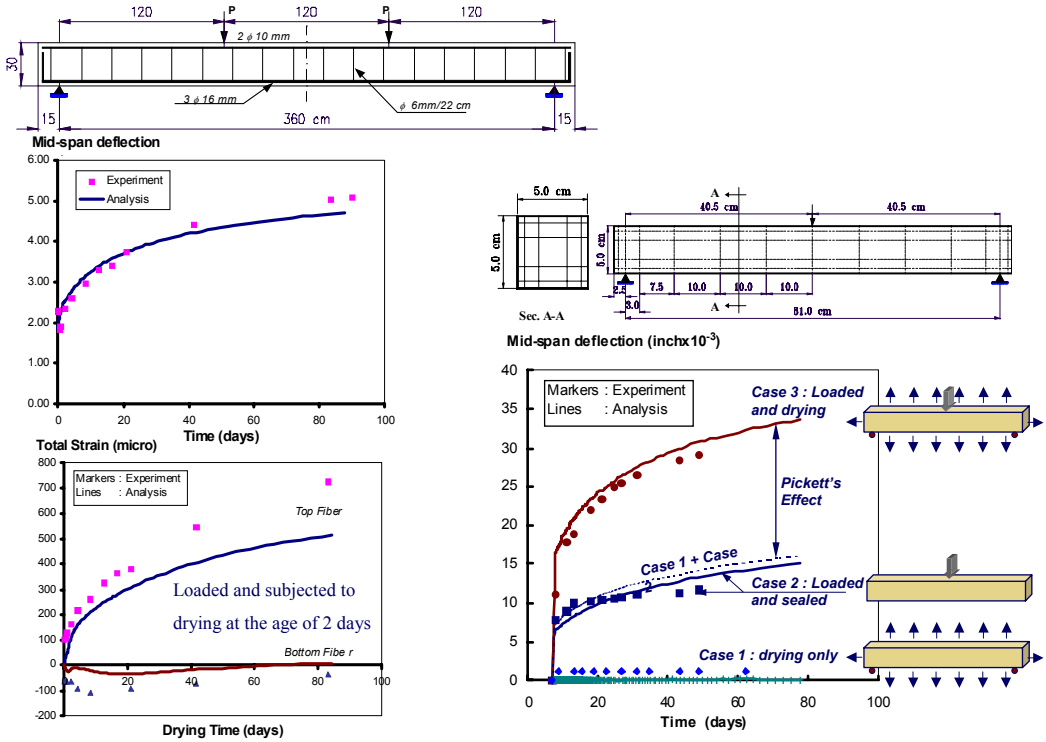

Fig. 38 Coupled sustained load and drying onto beams subjected to flexure.

The authors express their sincere gratitude to Prof. Hajime Okamura of Kochi University of Technology for his continuing supervision and Dr. Tsuyoshi Maruya of Taisei Corporation for valuable discussion and suggestions. Cooperation of Dr. Soltani Mohamad, Dr. Rasha Mabrouk and Mr. G. Zhu, research fellows (1999-2002) of the University of Tokyo, is deeply appreciated. This study was financially supported by JSPS Grant-in-aid for scientific research 14205065 and 14655160.

References

Bazant Z. P. and Prasannan S. (1989). "Solidification theory for concrete creep, I. Formulation, II. Verification and application" *Journal of Engineering Mechanics*, 115 (8), 1691-1725.

Broomfield, J.P. (1997). "*Corrosion of steel in concrete Understanding, investigation and repair*" London: E&FN SPON.

Freiser, H. and Fernando, Q. (1963). "*Ionic Equilibria in Analytical Chemistry*" New York: John Wiley & Sons, Inc.

Glucklich J. (1959). "Rheological behavior of hardened cement paste under low stress" *Journal of American Concrete Institute*, 56 (23), 327-337.

Gjørv, O. E. and Sakai, K. (1995) "Testing of chloride diffusivity for concrete", *In: Proc. of the International Conference on Concrete under Severe Conditions, CONSEC95*, 645-654.

Ishida, T., Chaube, R.P., Kishi, T. and Maekawa, K. (1998). "Modeling of pore water content in concrete under generic drying wetting conditions" *Concrete Library of JSCE*, 31, 275-287.

Ishida, T. (1999a). "*An integrated computational system of mass/energy generation, transport and mechanics of materials and structures*", Thesis (PhD). University of Tokyo (in Japanese).

Ishida, T., Chaube, R.P., Kishi, T. and Maekawa, K. (1999b). "Micro-physical approach to coupled autogenous and drying shrinkage of concrete" *Concrete Library of JSCE*, 33, 71-81.

Ishida, T. and Maekawa, K. (2000) "An integrated computational system for mass/energy generation, transport, and mechanics of materials and structures" *Concrete Library of JSCE*, 36, 129-144.

Ishida, T. and Maekawa, K. (2001) "Modeling of pH profile in pore water based on mass transport and chemical equilibrium theory" *Concrete Library of JSCE*, 37, 131-146.

Ishida, T. and Maekawa, K. (2002) "Solidified cementitious material-structure model with coupled heat and moisture transport under arbitrary ambient conditions", *Proceedings of fib congress 2002*, Osaka.

Kishi, T. and Maekawa, K. (1996). "Multi-component model for hydration heating of Portland cement" *Concrete Library of JSCE*, 28, 97-115.

Kishi, T. and Maekawa, K. (1997). "Multi-component model for hydration heating of blended cement with blast furnace slag and fly ash" *Concrete Library of JSCE*, 30, 125-139.

Mabrouk, R., Ishida, T. and Maekawa, K. (1998) "Solidification model of hardening concrete composite for predicting autogenous and drying shrinkage", *In*: E.

Tazawa Ed. *Autogenous Shrinkage of Concrete*. London: E&FN SPON, 309-318.

Mabrouk, R., Ishida, T., and Maekawa, K. (2000). "A unified solidification model of hardening concrete composite at an early age" *Proceedings of JCI*, 22 (2), 661-666.

Maekawa, K., Chaube, R. P., and Kishi, T. (1999). "*Modelling of Concrete Performance*" London: E&FN SPON.

Maekawa, K., Pimanmas, A. and Okamura, H. (2003). "*Nonlinear Mechanics of Reinforced Concrete*" London: Spon Press.

Maekawa, K. and Ishida, T. (2002) "Modeling of structural performances under coupled environmental and weather actions" *Materials and Structures*, 35, 591-602.

Maruya, T., Tangtermsirikul, S. and Matsuoka, Y. (1998). "Modeling of chloride ion movement in the surface layer of hardened concrete" *Concrete Library of JSCE*, 32, 69-84.

Neville AM. (1959) "Creep recovery of mortars made with different cements" *Journal of American Concrete Institute*, 56 (13), 167-174.

Nishi, T., Shimomura, T. and Sato, H. (1999). "Modeling of diffusion of vapor within cracked concrete" *Proceedings of JCI*, 21 (2), 859-864 (In Japanese).

Pickett, G. (1956). "Effect of aggregate on shrinkage of concrete and hypothesis concerning shrinkage", *Journal of ACI*, 52, 581-590.

Shimomura, T. and Maekawa, K. (1997) "Analysis of drying shrinkage behaviour of concrete using a micromechanical model based on the micropore structure of concrete" *Magazine of Concrete Research*, 49, No.181, 303-322.

Shimomura, T. (1998). "Modelling of initial defect of concrete due to drying shrinkage", *Concrete Under Severe Conditions 2, CONSEC 98*, **3**, (1998), 2074-2083.

Saeki, T., Ohga, H. and Nagataki, S. (1991). "Mechanism of carbonation and prediction of carbonation process of concrete" *Concrete Library of JSCE*, 17, 23-36.

Takeda, H. and Ishida, T. (2000). "Chloride equilibrium between chemically combined and adsorbed components in cementitious materials" *Proceedings of JCI*, 22 (2), 133-138.

Takegami, H., Ishida, T. and Maekawa, K. (2002) "Generalized model for chloride ion transport and equilibrium in blast furnace slag concrete" *Proceedings of JCI*, 24 (1), 633-638.

Uomoto, T. and Takada, Y. (1993). "Factors affecting concrete carbonation ratio" *Concrete Library of JSCE*, 21, 31-44.

Welty, J.R., Wicks, C.E., and Wilson, R.E. (1969). "*Fundamentals of momentum, heat, and mass transfer*" New York: John Wiley & Sons, Inc.

West, J.M. (1986). "*Basic Corrosion and Oxidation*" 2nd Ed. New York: John Wiley & Sons, 1986.

Yokozeki, K., Motohashi, K., Okada, K. and Tsutsumi, T. (1997) "A rational model to predict the service life of RC structures in marine environment", *Forth CANMET/ACI International Conference on Durability of Concrete*, SP170-40, 777-798.

Appendix

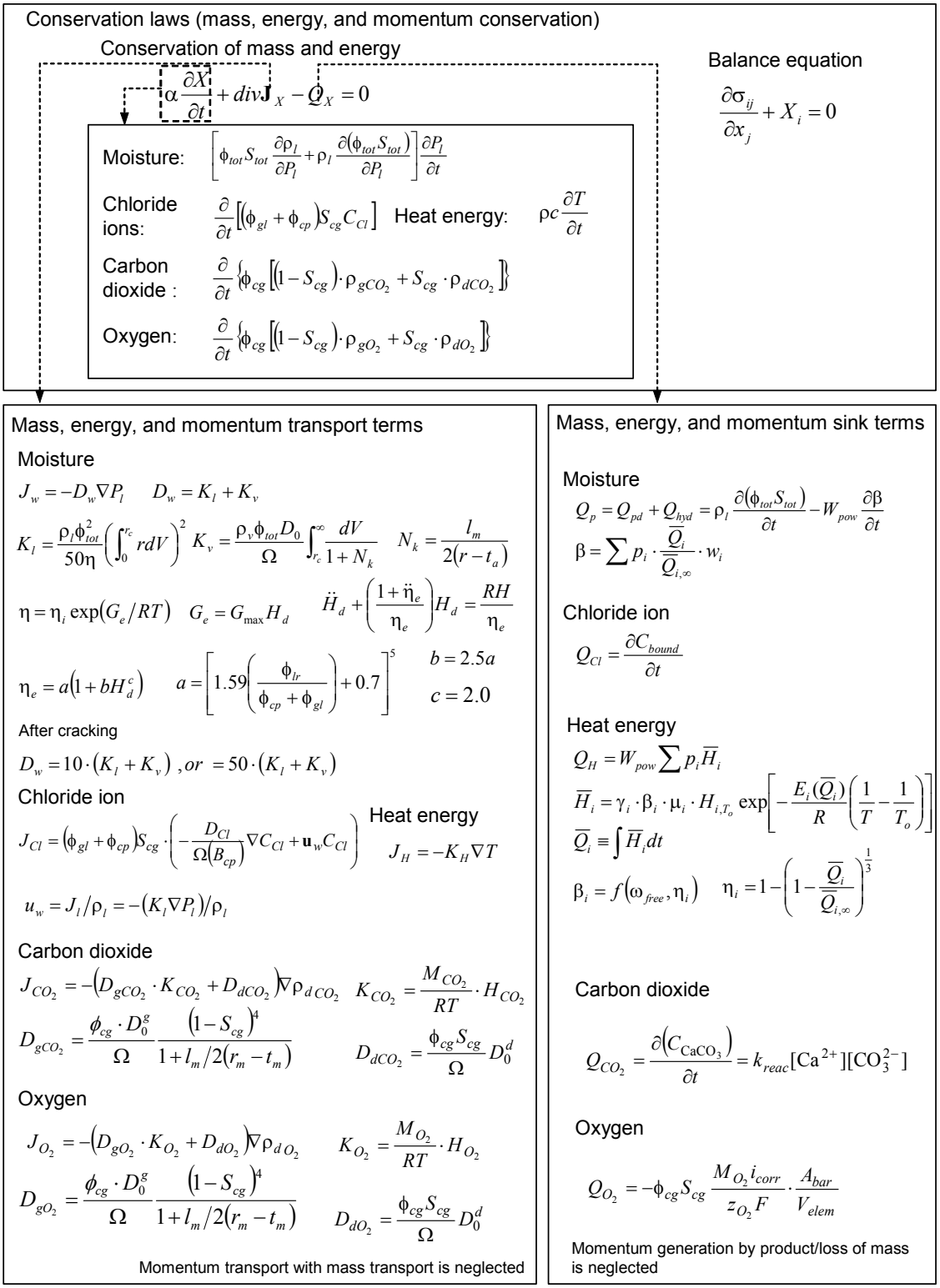

Fig. A Conservation laws, mass/energy transport, and sink term: Mass and energy conservation laws to govern the thermo-physics of materials, as well as the balance equations ruling mechanics of structures. These conservation laws must be satisfied in all material systems and so they apply to the field of concrete materials. Figure a also shows the mass, energy, and momentum transport terms, and sink term, for the above equations.

State, compatibility, and constitutive law of mass, energy, and solid

Thermodynamic equilibrium of mass

Moisture

$$P_l = \frac{\rho_l RT}{M_l}\ln RH = -\frac{2\gamma}{r_c}$$

$$t_a = \frac{0.525\times10^{-8}\cdot RH}{(1-RH/RH_m)(1-RH/RH_m+15RH)}$$

$$RH_m = \exp\left[\frac{-\gamma M_l}{\rho_l RT(r-t_a)}\right]$$

$$S_{ads} = \int_{r_c}^{\infty}\left[1-\left(\frac{r-t_a}{r}\right)^2\right]dV$$

$$S_{cnd} = \int_0^{r_c} dV = 1-\exp(-Br_c) = S_c$$

$$S_{lr} = RH$$

(*Wetting stage*)

$$S_{cnd} = S_c + \int_{r_c}^{\infty}\left(\frac{S_c}{V}\right)dV = S_c[1-\ln S_c]$$

$$S_{lr} = RH^{0.05}$$

(*Drying stage*)

$$S_{cnd} = S_c + \int_{r_c}^{\infty}\left(\frac{S_{r_{\min}}}{V}\right)dV = S_c - S_{r_{\min}}\ln S_c$$

$$S_{lr} = S_{\max}RH^{0.05}$$

(*Drying to wetting stage*)

$$S_{cnd} = S_c + \int_{r_c}^{r_{\max}}\frac{S_c}{V}dV = S_c[1+\ln S_{r_{\max}} - \ln S_c]$$

$$S_{lr} = 1+(RH-1)\left(\frac{S_{\min}-1}{RH_{\min}-1}\right)$$

(*Wetting to drying stage*)

$$S_{cg} = S_{ads} + S_{cnd}$$

$$S_{tot} = \frac{\phi_{lr}S_{lr} + (\phi_{gl}+\phi_{cp})S_{cg}}{\phi_{tot}}$$

$$\omega_{free} = \frac{\phi_{cp}S_{cp}(1-V_g)}{W_{pow}}$$

Chloride ion

$$C_{bound} = C_{chem} + \beta_{Cl}\cdot C_{Cl}$$

Carbon dioxide

$$\rho_{gCO_2} = \frac{M_{CO_2}}{RT}\cdot H_{CO_2}\cdot\rho_{dCO_2}$$

Oxygen

$$\rho_{gO_2} = \frac{M_{O_2}}{RT}\cdot H_{O_2}\cdot\rho_{dO_2}$$

Ion equilibria in pore solutions

$$H_2O \leftrightarrow H^+ + OH^-$$

$$H_2CO_3 \leftrightarrow H^+ + HCO_3^- \leftrightarrow 2H^+ + CO_3^{2-}$$

$$Ca(OH)_2 \leftrightarrow Ca^{2+} + 2OH^-$$

$$CaCO_3 \leftrightarrow Ca^{2+} + CO_3^{2-}$$

$$K_{sp}^1 = [Ca^{2+}][CO_3^{2-}] \quad K_{sp}^2 = [Ca^{2+}][OH^-]^2$$

$$K_w = [H^+][OH^-] \quad K_a = \frac{[H^+][HCO_3^-]}{[H_2CO_3]} \quad K_b = \frac{[H^+][CO_3^{2-}]}{[HCO_3^-]}$$

$$K_c = \frac{[Ca^{2+}][OH^-]^2}{[Ca(OH)_2]} = \frac{[Ca^{2+}]}{[Ca(OH)_2]}\cdot\frac{K_w^2}{[H^+]^2}$$

$$[H^+] + 2[Ca^{2+}] + 2[H_2CO_3]_s + [HCO_3^-]_s = [OH^-] + [HCO_3^-]_c + 2[CO_3^{2-}]_c$$

Electric potential of corrosion cell and current density equation

$$E_{Fe} = E_{Fe}^{\Theta} + (RT/z_{Fe}F)\ln h_{Fe^{2+}}$$

$$E_{O_2} = E_{O_2}^{\Theta} + (RT/z_{O_2}F)\ln(P_{O_2}/P^{\Theta})/h_{OH^-}^z = E_{O_2}^{\Theta} + (RT/z_{O_2}F)\ln(P_{O_2}/P^{\Theta}) - 0.06pH$$

$$E_0 = E_{O_2} - E_{Fe}$$

$$\eta^a = (2.303RT/\alpha z_{Fe}F)\log(i_a/i_0)$$

$$\eta^c = -(2.303RT/(1-\alpha)z_{O_2}F)\log(i_c/i_0)$$

$$i_L/z_{Fe}F = O_2^{sup} \qquad i_{corr} = i_L$$

$$R_{corr} = \phi S\frac{M_{Fe}\cdot i_{corr}}{z_{Fe}F}$$

Fig. B State and compatibility law of mass, energy, and solid (No.1): Figures B and C show the state, compatibility, and constitutive laws of mass, energy, and solid concrete. These equations are also modeled by considering the specific characteristics of concrete.

State, compatibility, and constitutive law of mass, energy, and solid

Pore structure formation

$$V_s = \frac{\alpha W_{pow}}{1-\phi_{ch}}\left(\frac{1}{\rho_p}+\frac{1}{\rho_w}\cdot\frac{\beta}{W_{pow}}\right) \qquad \phi_{lr} = \left(t_w s_l \rho_g\right)/2$$

$$\alpha = \sum p_i \cdot \left(\overline{Q}_i/\overline{Q}_{i,\infty}\right) \qquad \phi_{gl} = V_s\phi_{ch} - \phi_{lr}$$

$$\phi_{cp} = 1 - V_s - (1-\alpha)\frac{W_{pow}}{\rho_p} \qquad \phi_{tot} = \phi_{lr} + \phi_{gl} + \phi_{cp}$$

$$\rho_g = \rho_p\rho_w\left(1+\beta/W_{pow}\right)\left(1-\phi_{ch}\right)/\left(\rho_w+\beta\rho_p\right)$$

$$A\delta_m^3 + B\delta_m^2 + C\delta_m + D = 0$$

$$A = \{n(1-\phi_{in}) + 3(1-\phi_{ou})\}/\{3(n+3)\}$$

$$B = \{n(1-\phi_{in}) + 2(1-\phi_{ou})\}r_0/(n+2)$$

$$C = \{n(1-\phi_{in}) + (1-\phi_{ou})\}r_0^2/(n+1)^2$$

$$D = -(\alpha r_0^3/3)\left[\phi_{in} + \beta\rho_p/\rho_w\right]$$

Before contact

$$\phi_{ou} = 1.0$$

After contact

$$\phi_{ou} = 1-(X+Y)/Z \qquad \delta_{\max} = kr_o$$

$$X = -n(1-\phi_{in})\left[\frac{k^3}{3(n+3)}+\frac{k^2}{n+2}+\frac{k}{n+1}\right]$$

$$Y = \frac{\alpha}{3}\left[\phi_{in}+\beta\frac{\rho_p}{\rho_w}\right] \qquad Z = \frac{k^3}{n+3}+\frac{2k^2}{n+2}+\frac{k}{n+1}$$

$$s_l = 510 f_{pc} + 1500 f_{sg} + 3100 f_{fa}$$

$$\zeta = 19.0 f_{pc} + 1.5 f_{sg} + 1.0 f_{fa}$$

$$SA_c = \frac{3\delta_m}{\zeta r_{eq}^3(1-\phi_{in})}\left(A\delta_m^2 + B\delta_m + C\right)$$

$$SA_i = 2\phi_i\int_{r_m}^{\infty} B_i\exp(-B_i r)\,d\ln r \qquad SA_g = W_s \cdot sa_g$$

$$\phi(r) = \phi_{lr} + \phi_{gl}\cdot V_{gl} + \phi_{cp}\cdot V_{cp} \qquad V_i = 1-\exp(-B_i r)$$

Strength, elastic modulus, and deformability against pore pressure

$$f_c' = a\exp\left(-b\cdot V_{pore}\right) \quad a,b: \text{constant}$$

$$V_{pore} = \phi_{cp}\cdot\exp\left(-B_{cp}\cdot r_{50}\right) \quad r_{50} = 50\times10^{-9}[m]$$

$$E = 8.5\cdot10^3 f_c'^{1/3} \qquad f_t = 0.27 f_c'^{2/3}$$

Unrestrained strain due to temperature

$$\varepsilon_T = \alpha_c\Delta T$$

Unrestrained shrinkage strain due to pore pressure

$$\varepsilon_{sh} = \phi_{tot}S_{tot}f_{pow}\frac{P_l}{E_{sh}}$$

$$E_{sh} = E/3$$

Compatibility equation

$$\varepsilon_{xx} = \frac{\partial u}{\partial x} \qquad \varepsilon_{xy} = \frac{\partial v}{\partial x}+\frac{\partial u}{\partial y}$$

$$\varepsilon_{yy} = \frac{\partial v}{\partial y} \qquad \varepsilon_{yz} = \frac{\partial w}{\partial y}+\frac{\partial v}{\partial z}$$

$$\varepsilon_{zz} = \frac{\partial w}{\partial z} \qquad \varepsilon_{zx} = \frac{\partial u}{\partial z}+\frac{\partial w}{\partial x}$$

Constitutive law of solidifying concrete

$$\varepsilon_o = \rho_{ag}\varepsilon_{ag} + \rho_{cp}\varepsilon_{cp} \qquad \varepsilon_{cp} = f(\sigma_{cp})$$

$$\sigma_o = \rho_{ag}\sigma_{ag} + \rho_{cp}\sigma_{cp} \qquad \varepsilon_{ag} = \frac{1}{3.K_{ag}}\sigma_{ag}$$

$$\sigma_{cp}(t) = \int_{t'=0}^{t} S_{cp}(t',t)\,d\alpha(t')$$

$$\tau_o(t) = \int_{t'=0}^{t}\tau_o(t',t)\,d\alpha(t')$$

$$(1+\frac{E_v}{E_e})S(t) + \frac{C}{E_e}\frac{dS(t)}{dt} = E_v\overline{\varepsilon}'_{cp}(t) + C\frac{d\overline{\varepsilon}_{cp}(t)}{dt}$$

$$(1+\frac{G_v}{G_e})S_{ij}(t',t) + \frac{V}{G_e}\frac{dS_{ij}(t',t)}{dt} = G_v\cdot e'_{ij}(t',t) + V\frac{de'_{ij}(t',t)}{dt}$$

$$\sigma_{cp} = \sigma'_{cp} + \beta_f\cdot P_l$$

Fig. C State and compatibility law of mass, energy, and solid (No.2).

Table I shows input values needed for the calculation. In addition to the list in **Table I**, the x, y, and z-coordinates of each node and the element type/shape of the analytical target are required for the analysis. These input values determine the initial value at time=0, and also determine some of the material constants shown in **Table II**. Other material constants are taken from experimental results. By solving the above governing equations under given material constants and initial conditions, the variables shown in **Table III** are obtained in 3D space and the time domain.

Appendix **Table I** List of input values.

P_l	Initial pore pressure [Pa]	V_g	Aggregate volume per unit volume [kg/m^3]
C_{cl}	Initial concentration of Cl ions [mol/l]	f_{pc}	Weight fraction of Portland cement
T	Initial temperature [K]	f_{sg}	Weight fraction of blast furnace slag
ρ_{gCO_2}	Initial concentration of gaseous carbon dioxide [kg/m^3]	f_{fa}	Weight fraction of fly ash
ρ_{gO_2}	Initial concentration of gaseous oxygen [kg/m^3]	p_{sp}	Amount of organic admixture
p_i	Mass ratio of chemical component of cement (C_2S, C_3S, C_4AF, C3A, gypsum)	BF	Blain fineness index
ρ_p	Density of powder materials [kg/m^3]	A_{bar}	Surface area of reinforcement in a finite element
W/P	Water-to-powder ratio	V_{elem}	Volume of reinforcement in a finite element
W_{pow}	Powder weight per unit volume [kg/m^3]		

Table II List of material constant.

ρ_l	Density of liquid [kg/m^3]	$\overline{Q}_{i,\infty}$	Maximum theoretical specific heat of component i [kcal]
ρ_v	Density of saturated vapor [kg/m^3]	W_{pow}	Powder weight per unit volume [kg/m^3]
ρc	Heat capacity [kcal/K.m^3]	γ_I	Reduction factor representing the retardation effect on hydration of fly ash and organic admixture
D_0	Vapor diffusivity in free atmosphere [m^2/s]	μ_i	Coefficient representing the effect of mineral composition (C_3S, C_2S) on hydration rate
D_{cl}	Chloride ion diffusivity in pore solution phase [m^2/s]	T_0	Reference temperature (=293 K)
D_0^g	Diffusivity of CO_2 in a free atmosphere	R	Gas constant [J/mol.K]
D_0^d	Diffusivity of dissolved CO_2 in pore water	k_{reac}	Reaction rate coefficient of carbonation
H_{CO2}	Henry's constant for carbon dioxide	$\boldsymbol{K_w}$	Equilibrium constant of concentration for water dissociation
M_{CO2}	Molecular mass of carbon dioxide	K_a	Equilibrium constant of concentration for dissociation of H_2CO_3 and HCO_3^- [mol/l]
Ω	Parameter representing tortuosity of pore ($=(\pi/2)^2$)	K_b	Equilibrium constant of concentration for dissociation of HCO_3^- and CO_3^{2-} [mol/l]
η_i	Viscosity under ideal conditions [Pa.s]	K_c	Equilibrium constant of concentration for dissociation of $Ca(OH)_2$ [mol/l]
l_m	Mean free path of a gas molecule [m]	K_{sp}^1	Solubility-product constant of the calcium carbonate [mol]
G_{max}	Maximum additional Gibbs energy for the activation of flow (=3500kcal/mol)	K_{sp}^2	Solubility-product constant of the calcium hydroxide [mol]

K_H	Heat conductivity [kcal/K.m.sec]	F	Faraday constant [C/mol]
p_i	Mass ratio of chemical component i of cement	z_{Fe}	Number of electric charge of Fe
w_i	Amount of water consumed by chemical component i due to hydration [mol/mol]	z_{O2}	Number of electric charge of oxygen
E^{Θ}_{Fe}	Referential standard cell potential of Fe at 25C (V, SHE)	ζ	Ratio of volume to the external surface area of a typical hydrate products [nm]
E^{Θ}_{O2}	Referential standard cell potential of O_2 at 25C (V, SHE)	f_{pc}	Weight fraction of Portland cement
P^{Θ}	Atmospheric pressure	f_{sg}	Weight fraction of blast furnace slag
M_{Fe}	Molecular mass of Fe	f_{fa}	Weight fraction of fly ash
i_0	Exchange current density	t	Equivalent spherical cell radius [m]
ρ_p	Density of powder materials [kg/m^3]	sa_g	Specific surface area of hydrates [m^2/kg]
ρ_w	Density of chemically hydrated products [kg/m^3]	r_m	Minimum radius of pores [m]
ϕ_{in}	Specific porosity of inner products (=0.28)	M_l	Molecular mass of liquid [kg/mol]
t_w	Thickness of interlayer porosity (=2.8×10^{-10}[m])	γ	Surface tension of liquid [N/m]
s_l	Specific surface area of interlayer porosity [m^2/kg]	V_g	Volume of aggregate per unit volume [m^3/m^3]
N	Parameter representing a generic pattern of deposition of products around particle	f_{pow}	Coefficient of linear expansion of concrete [1/K]
R_0	Radius of powder particle [m]	ν	Poisson's ratio

Table III List of variables.

T	Time [s]	η_e	Effective non-ideal viscosity of the pore fluid[N·s/m^2]
P_l	Pore pressure [Pa]	G_e	Additional energy for activation of flow
C_{cl}	Concentration of chloride ions [mol/l]	H_d	Fictitious humidity parameter
T	Temperature [K]	r	Pore radius [m]
ρ_{gCO2}	Concentration of gaseous carbon dioxide [kg/m^3]	r_c	Pore radius in which the equilibrated interface of liquid and vapor is created [m]
ρ_{dCO2}	Concentration of dissolved carbon dioxide [kg/m^3]	V	Normalized pore volume [m^3/m^3]
ρ_{gO2}	Concentration of gaseous oxygen [kg/m^3]	N_k	Knudsen number
ρ_{dO2}	Concentration of dissolved oxygen [kg/m^3]	$\mathbf{u}_w$	Velocity vector of pore solution phase
J_w	Flux of moisture [kg/m^2.s]	J_l	Flux of liquid [kg/m^2.s]
J_{cl}	Flux of chloride ions [mol/m^2.s]	D_{gCO2}	Diffusion coefficient of gaseous CO_2 in a porous medium [m^2/s]
J_H	Flux of heat [kcal/m^2.s]	D_{dCO2}	Diffusion coefficient of dissolved CO_2 in a porous medium [m^2/s]
J_{CO2}	Flux of gaseous and dissolved carbon dioxide [kg/m^2.s]	D_{gO2}	Diffusion coefficient of gaseous O_2 in a porous medium [m^2/s]
J_{O2}	Flux of gaseous and dissolved oxygen [kg/m^2.s]	D_{dO2}	Diffusion coefficient of dissolved O_2 in a porous medium [m^2/s]

D_w	Moisture conductivity [kg/Pa.m.s]
K_l	Liquid conductivity [kg/Pa.m.s]
K_v	Vapor conductivity [kg/Pa.m.s]
η	Viscosity of fluid under non-ideal conditions [N·s/m^2]
Q_{cl}	Term representing the reduction of free chlorides
Q_{Cl}^{cb}	Term representing the extrication of bounded chlorides due to carbonation
Q_{CO2}	Term representing the consumption rate of carbon dioxide
Q_{O2}	Term representing the consumption rate of oxygen
β	Amount of chemical combined water per unit weight of hydrated powder materials [kg/kg]
$\overline{Q}_i$	Accumulated heat generation of chemical component *i* [kcal]
$\overline{H}_i$	Heat generation rate of clinker component *i* [kcal/kg.s]
$H_{i,To}$	Reference heat rate of *i*-th component at temperature T_o [kcal/kg.s]
$E_i(\overline{Q}_i)$	Activation energy of component *i* [kcal.K/kg.s]
β_i	Reduction of probability of contact between unhydrated compounds and free pore water
ω_{free}	Amount of free water
η_i	Non-dimensional thickness of cluster
V_s	Volume of hydrated products [m^3/m^3]
W_s	Weight of hydrated products [kg/m^3]
α	Average degree of hydration
ρ_g	Dry density of gel products [kg/m^3]
ϕ_{cp}	Capillary porosity
ϕ_{gl}	Gel porosity
ϕ_{lr}	Interlayer porosity
ϕ_{tot}	Total porosity
ϕ_{ou}	Porosity at outermost boundary of the expanding cluster
δ_m	Cluster thickness
SA_c	Specific surface area of capillary porosity [m^2/m^3]
SA_g	Specific surface area of gel porosity [m^2/m^3]
B_i	Porosity distribution parameter
Q_H	Heat generation term
Q_p	Sink term for moisture balance
Q_{pd}	Term representing bulk porosity change effects
Q_{hyd}	Term representing water consumption due to hydration
S_c	Degree of saturation due to condensed water in virgin wetting path
r_{max}	Pore radius of the largest pores that experienced a complete saturation in the wetting history [m]
S_{rmax}	Highest saturation experienced by the porous media in its wetting history
r_{min}	Pore radius of the smallest pores that experience emptying out in the drying history [m]
S_{rmin}	Lowest saturation of porous media in its wet-dry history
S_{max}	Highest saturation experienced by interlayer porosity in its wetting history
S_{min}	Lowest saturation experienced by interlayer porosity in its drying history
RH_{min}	Minimum RH experienced in its drying history
S_{cg}	Degree of saturation of gel and capillary pores
S_{lr}	Degree of saturation of interlayer porosity
S_{tot}	Degree of saturation of total pores
C_{bound}	Amount of bound chlorides [mol/l]
C_{chem}	Amount of chemically bounded chlorides [mol/l]
β_{Cl}	Equilibrium coefficient of free and bound chlorides
C_{CaCO3}	Concentration of $CaCO_3$ [mol/l]
i_{corr}	Current density of corrosion cell [A/m^2]
E_{Fe}	Standard cell potential of Fe (V, SHE)
E_{O2}	Standard cell potential of O_2 (V,SHE)
E_0	Electric potential of corrosion cell (V)
η^a	Charge transfer at anode [V]
η^c	Charge transfer at cathode [V]
I_a	Current density at anode [A/m^2]
i_c	Current density at cathode [A/m^2]
i_L	Limit current density under O2 diffusion control [A/m^2]
ε_{sh}	Unrestrained shrinkage strain due to pore pressure

RH	Relative humidiry	E_{sh}	Deformability against capillary stress [Pa]
t_a	Thickness of adsorbed layer [m]	f_c'	Compressive strength [Pa]
RH_m	Humidity required to fully saturate a pore	V_{pore}	Volume of capillary pores above 50nm
S_{ads}	Degree of saturation due to adsorbed water	E	Elastic module [Pa]
S_{cnd}	Degree of saturation due to condensed water	f_t	Tensile strength [Pa]
X_i	External force in *i*-direction	K_{ag}	Volumetric stiffness of aggregate
u	Displacement in x-direction	ε_0	Mean volumetric strain on concrete
v	Displacement in y-direction	σ_0	Mean volumetric stress of concrete
w	Displacement in z-direction	ε_{ag}	Mean volumetric strain on aggregate
ε_T	Unrestrained strain due to temperature	ε_{cp}	Mean volumetric strain on cement paste
σ_{cp}	Mean volumetric stress of cement paste	σ_{ag}	Mean volumetric stress of aggregate